Control of CO2 on flow and reaction paths in olivine-dominated basements: An experimental study

Steve Peuble, Marguerite Godard, Philippe Gouze, Richard Leprovost, Isabelle Martinez, Svetlana Shilobreeva

HAL Id: hal-02083060
https://hal.umontpellier.fr/hal-02083060

Submitted on 6 Nov 2020

1   **Revision 2**

2

3   **Control of CO$_2$ on flow and reaction paths in olivine-dominated basements: an**

4   **experimental study**

5

6   Steve Peuble[1*], Marguerite Godard[1], Philippe Gouze[1], Richard Leprovost[1], Isabelle Martinez[2]

7   and Svetlana Shilobreeva[3]

8
9
10
11   *[1] Géosciences Montpellier, Université de Montpellier, CNRS, Place Eugène Bataillon cc060,*

12   *F-34095 Montpellier Cedex 5, France*

13

14   *[2] Institut de Physique du Globe de Paris, Sorbonne Paris Cité, Université Paris-Diderot,*

15   *UMR 7154 CNRS, 75238 Paris, France*

16
17   *[3] Vernadsky Institute of Geochemistry and Analytical Chemistry of Russian Academy of*

18   *Sciences, Moscow, Russia*

19
20
21

22

23

24

25

26

27

28

29

30   **Corresponding author.*

31   *Steve Peuble*

32   Now at : *Mines Saint-Etienne, Univ Lyon, Univ Jean Moulin, Univ Lumière, Univ Jean*

33   *Monnet, ENTPE, INSA Lyon, ENS Lyon, CNRS, UMR 5600 EVS, UMR 5307 LGF, Centre*

34   *SPIN, Département PEG, F - 42023 Saint-Etienne, France*

35   *Email: steve.peuble@mines-stetienne.fr*

36

Abstract

The objective of this paper is to quantify the mass transfers involved in the hydrothermal alteration of olivine-rich peridotites in the presence of CO_2-enriched waters, and to determine their effects on the rock hydrodynamic properties. Three flow-through experiments were performed at a temperature of 185 °C and a total pressure of 22.5 ± 2.5 MPa. They consisted in injecting a hydrothermal fluid with different concentrations of carbon dioxide (CO_2 = 6.26, 62.6 and 659.7 mmol.L^{-1} i.e. pCO_2 = 0.1, 1 and 10 MPa, respectively) into cylinders of sintered San Carlos (Arizona, USA) olivine grains. The results show that for low pCO_2 conditions (from 0.1 to 1 MPa), olivine is mainly altered into hematite and Mg(Fe)-rich phyllosilicates. Such iddingsitic-type assemblages may clog most of the rock flow paths, resulting in a strong decrease in permeability. Rare Ca-Fe-carbonate minerals also precipitated under these conditions despite the initial Mg-rich system. For higher pCO_2 conditions (~10 MPa), olivine is more efficiently altered. A greater amount of poorly crystallized Fe(Mg)-rich phyllosilicates and magnesite is produced, and the carbonation rate of olivine is 3 to 11 times higher than when the pCO_2 is 10 to 100 times lower. Interestingly, the changes in porosity caused by the formation of carbonated and hydrous minerals are small while a strong decrease in permeability is measured during the experiments. The formation of reduced carbon is also observed. It is located preferentially at the inlet, where pH is the lowest. This testifies to a competition between reduction (probably associated with the oxidation of ferrous iron) and carbonation; two processes involved in the fixation of CO_2 in a mineral form. One may speculate that the formation of reduced carbon can also be a significant mechanism of CO_2 sequestration in olivine-dominated basements.

1. Introduction

Carbonation of mafic and ultramafic rocks (mainly basalts and peridotites) is a widespread process in nature for example, in the past and present oceanic crust and mantle exposed on the seafloor (e.g., Nakamura and Kato, 2004; Ludwig et al., 2006) and within ophiolites (Matter and Kelemen, 2009; Noël et al., 2018). It occurs through the interaction of carbon dioxide (CO_2) with divalent metal ions (Mg^{2+}, Fe^{2+}, Ca^{2+}) contained in mafic silicates (e.g., olivine) to precipitate solid carbonate minerals and quartz (e.g., Oelkers et al., 2008):

$$(Mg_{1.80}Fe_{0.20})SiO_4 + 2\ CO_2 = 2\ (Mg_{0.90}Fe_{0.10})CO_3 + SiO_2 \qquad (1)$$

Olivine (Fo$_{90}$)   *Mg-carbonates*   *Quartz*

Natural carbonation of mafic and ultramafic basements controls part of the Earth's carbon cycle by contributing to the uptake of CO_2 deriving, for example, from the atmosphere, magmatic degassing and C-bearing mineral leaching (Zeebe and Caldeira, 2008; Coggon et al., 2010; Dasgupta and Hirschmann, 2010; Rausch et al., 2013; Kelemen and Manning, 2015). CO_2 mineral trapping in mafic and ultramafic aquifers is also envisioned as a safe way for mitigating carbon anthropogenic emissions to the atmosphere (e.g., Seifritz, 1990). This method is being experimented on a large scale via different pilot sites of CO_2 injection into basaltic reservoirs (Gislason et al., 2010; McGrail et al., 2011).

In both natural and industrial CO_2 geological storage sites, carbon trapping will depend on the mass transfer of solute reactants (products) to (from) reaction interfaces. However, modeling the coupled effects of reactive transport mechanisms during *in situ* mineralization of CO_2 in (ultra-)mafic aquifers is challenging because of the complexity of natural systems and the lack of experimental characterization of the effective mechanisms. Most of the laboratory CO_2 mineralization experiments are conducted in closed reactors (i.e. with no renewing of the solute) and high water-rock ratios (Pokrovsky and Schott, 2000; Giammar et al., 2005; Hänchen et al., 2006; Hänchen et al., 2008; Daval et al., 2011; Kelemen et al., 2011; Klein and McCollom, 2013; Sissmann et al., 2014). Conversely, aquifers are known to be dynamic systems where local chemical equilibria between fluids and minerals are controlled by low water-rock ratios and pore-scale fluid flow (e.g., Steefel et al., 2005). Extensive outcrops of weathered peridotites show different forms and degrees of CO_2 mineralization based on local geological contexts i.e. on small scale variations in the chemistry and hydrodynamic rock properties: carbonates may form large chimneys in deep-sea hydrothermal sites (e.g., Ludwig et al., 2006), travertine deposits from springs in peridotite catchments (Kelemen and Matter, 2008), but also geometrical veins through partially hydrated (Noël et al., 2018) to fully

106 carbonated peridotites, such as ophicalcite (Bernoulli and Weissert, 1985; Schwarzenbach et

107 al., 2013) and listvenite (Hansen et al., 2005; Nasir et al., 2007).

108 In agreement with these natural analogues, some recent reactive percolation experiments

109 conducted on ultramafic cores pointed out the role of fluid flow velocity and pore geometry

110 on the nature and rate of carbonation reactions by controlling chemical microenvironments at

111 the pore scale (Andreani et al., 2009; Godard et al., 2013; Peuble et al., 2015a; Peuble et al.,

112 2015b; Luhmann et al., 2017b). Olivine was proposed to be preferentially dissolved in high

113 flow areas facilitating high fluid-rock disequilibrium conditions while carbonates precipitate

114 mostly in reduced flow zones where diffusion-dominated transport favors the mixing of

115 reactants and their high residence time in the vicinity of the reaction zone (Andreani et al.,

116 2009). Similarly, Peuble et al. (2015b) reported that carbonates grow perpendicular to the

117 main fluid flow direction i.e. where the fluid velocity field tends toward zero promoting

118 cationic supersaturation conditions. Chemical microenvironments may vary in space and time

119 within a porous aquifer depending on its structure, flow paths and successive dissolution-

120 precipitation reactions. For instance, the pH of the fluid increases during its percolation in

121 olivine cores leading to changes in secondary mineralogy marked by the replacement of

122 carbonates by serpentine-type minerals (Peuble et al., 2015b). Likewise, a lateral and

123 temporal variation of CO_2 concentration may also control fluid-rock interaction reactions.

124 Hänchen et al. (2008) observed that the transformation of olivine into magnesite under a

125 partial pressure of CO_2 (pCO_2) of 0.1 MPa and a temperature of 120 °C is slowed down by

126 intermediate reactions: it occurs through the destabilization and/or dissolution of

127 hydromagnesite which itself nucleates from brucite. On the other hand, olivine can be directly

128 dissolved into magnesite at a pCO_2 of 10 MPa for similar temperature conditions (Hänchen et

129 al., 2008). This would induce significant changes in reaction pathways within mafic and

130 ultramafic reservoirs permeated by CO_2 influxes, as CO_2 injection wells in the context of C-

131 sequestration industrial sites.

132 In turn, carbonate formation is likely to have negative feedback effects on fluid flow by

133 decreasing the porosity and permeability of the rock (Oelkers et al., 2008; Jun et al., 2013;

134 Peuble et al., 2015b). The alteration of olivine-dominated basements into carbonates is

135 considered as a volume-increasing process since the volumetric mass density of products

136 (e.g., 3.0 g.cm^{-3} for magnesite) is lower than that of reactants (e.g., 3.3 g.cm^{-3} for olivine)

137 (Deer et al., 1992). As a result, the further carbonation of mafic silicates will rely on cracks,

138 induced by tectonic stresses (Andreani et al., 2007) or by crystal-growth (Jamtveit et al.,

139 2008; Rudge et al., 2010; Kelemen and Hirth, 2012), to preserve fluid pathways in the host

140 rock unless reaction products are leached out by the fluid flow to maintain pore volume and

141 permeability at reaction interfaces (Godard et al., 2013; Peuble et al., 2017).

142   Defining the main parameters controlling the development of one suite of chemical and

143 mineralogical reactions at the expense of another, but also their feedback effects on

144 hydrodynamic rock properties is therefore challenging in systems as complex as natural

145 geological porous media where temperature, pressure, composition and permeability will

146 change along flow paths. Numerical simulations allow to integrate the role of coupling

147 between chemistry, transport and fluid flow e.g., JChess geochemical code (Van der Lee et

148 al., 2003) or PhreeqC geochemical code (Parkhurst and Appelo, 2013). However, these

149 modelling tools are designed to handle transport at the Darcy's scale for which the primary

150 upscaling of the flow and transport is implicitly performed. This implies that the local spatial

151 variability of the velocity field (controlled by the Stokes flow) inherent to the geometrical

152 heterogeneity of the connected porosity as well as the local mineralogical heterogeneity are

153 averaged into volumes, named as Representative Elementary Volumes (REV) encompassing

154 several pores. For instance, these models assume (*i*) a full mixing of solutes at the REV scale

155 and comprehensibly a full accessibility of all reactants to reactive surfaces, and (*ii*) a constant

156 residence time of chemical species into the entire REV. The results of the flow-through

157 experiments cited above indicate clearly that these assumptions cannot be considered a priori,

158 i.e. that pore scale heterogeneities are often controlling overall mass transfers for the space

159 and time characteristics under consideration. Yet, the scarcity of experimental data compared

160 to the large variability of potentially realistic situations makes the derivation of reliable

161 upscaling models challenging. For example, it is critical to study the functional dependencies

162 between chemical, hydrodynamic and mechanical processes for experimental configurations

163 with low degree of freedom, in order to characterize the role of surface processes and kinetics

164 versus equilibrium (Pokrovsky and Schott, 2000; Bearat et al., 2006; Daval et al., 2013).

165   In this paper, we present and discuss the results of three reactive percolation experiments

166 conducted on sintered olivine cores at various CO_2 partial pressure (*pCO_2*). All other

167 characteristics are similar for the three experiments. The objective of this study is to

168 investigate olivine alteration processes under different *pCO_2* in order to reproduce the

169 conditions close and far from a CO_2 inflow percolating an ultramafic setting. We aim to

170 characterize the mechanisms controlling fluid chemistry, secondary mineralogy and their

171 consequences on the hydrodynamic rock properties (i.e. porosity and permeability) in the

172 context of CO_2-fluids interactions with ultramafic rocks. Results are compared to previous

173　experimental studies and discussed in the context of natural and anthropically induced

174　hydrothermal systems in ultramafic rocks.

175

176　**2. Methodology**

177

178　*2.1. Experimental protocol*

179

180　Three reactive percolation experiments were performed using the Icare Lab 3 reactive

181　flow-through system (ICARE-RFTS3, Geosciences Montpellier). They were conducted under

182　similar conditions of flow injection rate (0.5 mL.h^{-1}), temperature (185 °C) and average

183　pressure (22.5 ± 2.5 MPa), but with setting the pCO_2 of the injected fluid at 0.1, 1 and 10 MPa

184　respectively in order to investigate only the effect of changes in CO_2 concentration on fluid-

185　rock interactions.

186　The ICARE-RFTS3 experimental device allows the injection of solutes through

187　permeable samples over the range of pressure and temperature conditions expected in

188　hydrothermal systems and in geological reservoirs targeted for CO_2 sequestration: $P = 0.5 -$

189　40 MPa and $T = 50 - 400$ °C. It is built for exploring mass transfer processes from kinetic-

190　controlled to transport-controlled conditions for samples displaying permeability values

191　ranging from 10^{-20} to 10^{-13} m^2.

192　ICARE-RFTS3 (Fig. 1) includes (*i*) a fluid injection system, comprising three computer-

193　controlled motorized dual-piston pumps programmed to achieve the mixing of CO_2 with

194　water and then inject the mixture through the sample at a constant flow rate, (*ii*) a heated

195　sample-holder, maintaining the sample at the given confinement pressure using a motorized

196　piston pump, (*iii*) a back pressure controller equipment, composed of a motorized piston

197　pump coupled with a large volume pneumatic dumper, and (*iv*) an automatic sampling system,

198　allowing to sample ≈ 3 mL of fluid directly from the rock sample outlet. All surfaces of the

199　ICARE-RFTS3 system in contact with the fluid are made of Hastelloy C22. The motorized

200　piston pumps are equipped with displacement encoders allowing an accurate control of the

201　flow injection rate; fluctuations are less than 0.1% of the flow injection rate. Continuous flow

202　rates ranging from 3.4×10^{-3} to 10^2 mL.h^{-1} ($9.5 \times 10^{-13} - 2.8 \times 10^{-8}$ m^3.s^{-1}) can be operated.

203　All pumps, valves and the sampling system are controlled by a LabView® program according

204　to the user requirements. Both axial and radial confining pressures are applied to the sample

205　fitted into a tight Teflon sleeve. The confinement pressure is set to 112% of the inlet fluid

206　pressure during the experiments (from the loading to the unloading of the circuit fluid

207 pressure) in order to minimize deviatoric stresses. During reactive percolation experiments, a
208 porous nickel sinter is positioned upstream of the sample to ensure a homogeneous
209 distribution of the flow.

210 The difference in fluid pressure between the inlet and the outlet of the sample, ΔP (in Pa),
211 is monitored during the experiments using a differential pressure sensor (Rosemount® 3051
212 with an accuracy of 3×10^3 Pa) coupled with two high-resolution pressure sensors (Keller®
213 PA-33x with an accuracy of 3.5×10^4 Pa). Assuming laminar flow conditions, the sample
214 permeability k (in m²) was calculated from Darcy's law:

$$k = \frac{Q.\mu.L}{S.\Delta P} \tag{2}$$

215 where Q is the flow injection rate (m^3.s^{-1}), L and S the length (m) and section area (m²) of
216 the sample, respectively, and μ is the dynamic fluid viscosity set at 1.5×10^{-4} Pa.s for water at
217 185 °C (Mao and Duan, 2009).

218

219 *2.2. Preparation and composition of olivine cores and injected fluids*

220

221 The percolation experiments were performed on cores ($\approx$ 16 mm length $\times$ 6.35 mm
222 diameter) made of sintered San Carlos (Arizona, USA) olivine grains. The sintering technique
223 was used because it allows obtaining solid aggregates of controlled porosity and composition
224 (Table 1 and Appendix A1).

225 The starting material consisted of millimeter-size grains of San Carlos olivine (Fo$_{90}$, see
226 Appendix A1). Olivine grains were sorted under binocular microscope to eliminate those
227 having spinels or pyroxenes on their surfaces or as inclusions. The selected grains were
228 crushed and sieved. The 100 – 150 µm olivine fraction was then cleaned ultrasonically for 10
229 min in diluted hydrochloric acid ($\approx$ 2% HCl) to remove any carbonate grains and finally
230 rinsed in MilliQ-water for 15 min. The cleaning and rinsing procedure was repeated three
231 times before drying the powder at 110 °C for 12 hours. Bulk composition of the resulting
232 olivine powder was analyzed by X-ray fluorescence spectroscopy (Geolabs, Canada) and
233 compared to the composition of the olivine grains measured by electron probe micro-analyzer
234 (EPMA, University of Montpellier; Appendix A1). Bulk and mineral compositions were
235 similar indicating that no contamination occurred during the preparation procedure.

236 Three sintered olivine cores were made using the following procedure. First, the 100 –
237 150 µm fraction of the cleaned olivine powder was pressed at 5 MPa and 25 °C in stainless
238 steel capsules. Then, samples were sintered at a temperature of 1180 °C and a confining

pressure of 150 MPa using a gas medium (Ar) high-pressure and high-temperature vessel (Paterson, 1990) at Geosciences Montpellier. For each core, the initial porosity was measured before the percolation experiment using the triple weight method (Dullien, 1979); it ranged between 10.57 and 11.30 ± 0.10% (Table 1). Experiments were performed on samples named SC1-L, SC2-M and SC3-H, which have similar initial permeability ($1.6 - 4.6 \times 10^{-15}$ m^2; Table 1).

The inlet fluid was a mineral water (Volvic®) mixed with various concentrations of gaseous CO_2. The Volvic® water was selected because of its chemical composition that is stable and typical of aquifers containing mafic minerals (e.g., olivine) under low temperature conditions (50 – 200 °C; Table 2 and Appendix A2). The rationale was to reproduce chemical conditions similar to those anticipated for CO_2 industrial storage in igneous basements, close and far from an injection site. The Volvic® water was first vacuumed for three hours at room temperature to degas it and thus reproduce anoxic conditions. Then it was mixed with gaseous CO_2 at 30 MPa and 25 °C by repeated back-and-forth pumping between two out of the three injection pumps for three hours (Fig. 1). The pH of Volvic® water at 25 °C is 7.0. After mixing with CO_2, the inlet fluid pH at 185 °C and 22.5 ± 2.5 MPa was calculated using PhreeqC and the Lawrence Livermore National Laboratory 'thermo.com.V8.R6.230' thermodynamic database (Parkhurst and Appelo, 2013): pH = 4.5, 3.9 and 3.4 for the experiments SC1-L (experiment at the lowest pCO_2 = 0.1 MPa; CO_2 = 6.26 mmol.L^{-1}), SC2-M (experiment at medium pCO_2 = 1 MPa; CO_2 = 62.6 mmol.L^{-1}) and SC3-H (experiment at the highest pCO_2 = 10 MPa; CO_2 = 659.7 mmol.L^{-1}), respectively.

2.3. Analytical methods

The chemical composition of the inlet and outlet fluids was measured on an Agilent 7700x inductively coupled plasma – mass spectrometer (ICP–MS) at Geosciences Montpellier (AETE platform, France). All fluids were previously diluted by two in an acidified MilliQ-water (≈ 2% of nitric acid). Indium (1 ppb) was used as an internal standard during analyses. Both accuracy and reproducibility of the measurements were assessed with the SLRS-5 water standard. The analytical results were within the range of compiled values (Yeghicheyan et al., 2013). The external reproducibility was better than 5% for all measured elements. The Si, Mg, Fe and Ca concentrations of the inlet and outlet fluids and of the SLRS-5 water standard are reported in Table 2 and in the Supplementary Materials (Appendix A3).

Both composition and mineralogy of the reacted aggregates were characterized with the methodology described thereafter. Samples magnetic susceptibility was measured before and after each experiment on a Bartington–MS2 meter susceptibility system operating at 0.565 kHz for values ranging from 1×10^{-8} to 9999×10^{-8} $m^3.Kg^{-1}$ with an uncertainty of $\approx 1\%$ (Geosciences Montpellier).

After magnetic susceptibility measurements, the reacted cores were longitudinally sawn into two semi-cylindrical halves. The first half was polished for microscopic and spectroscopic characterizations (scanning electron microscopy, Raman spectroscopy and electron probe micro-analyzer) according to the protocol described in detail in Peuble et al. (2015a). The second half was crushed for bulk powder analyses (Mössbauer spectroscopy and bulk rock carbon and hydrogen measurements).

Polished sections were described optically, then backscattered (BSE) and secondary electron (SE) images were collected on a FEI Quanta FEG 200 scanning electron microscope (SEM) using an acceleration voltage of 15 kV and an ambient pressure of 0.45 torr (University of Montpellier, France).

Secondary minerals have been also identified on LabRam Aramis IR2 (Charles Gerhardt Institute, Montpellier, France) and XploRa (Laboratory of Geology of Lyon, France) confocal Raman spectrometers (Jobin-Yvon SA, Horiba, France); both equipped with a charge-coupled device (CCD) detector. Raman analyses were performed with 473 nm (LabRam Aramis IR2) and 532 nm (XploRa) radiations from diode lasers generating less than 1 mW. The spectra resolution is $\pm$ 2 cm^{-1}. Before analyses, Raman spectrometers were calibrated using a crystalline silicon thin-section showing a large band at 521 ± 2 cm^{-1}.

The composition of primary and secondary minerals was measured on carbon-coated polished sections (thus precluding further investigations on C-phases) using a Cameca SX-100 EPMA (University of Montpellier) equipped with five wavelength-dispersive X-ray spectrometers (WDS). Analyses were done at an acceleration potential of 20 kV and a beam current of 10 nA. Results are summarized in Appendix A1.

The presence (or lack) of ferric iron in the reacted samples was measured by Mössbauer spectroscopy at the Charles Gerhardt Institute (Montpellier, France) with a detection limit of $\approx 2\%$. Mössbauer data were acquired at ambient temperature on ≈ 200 mg bulk rock powders in the constant acceleration mode. [57]Fe Mössbauer spectra were obtained using a source of [57]Co in rhodium metal. The spectrometer was operated using a triangular velocity waveform. Gamma rays were detected with a NaI scintillation detector. Spectra were fitted with a combination of Lorentzian lines then used to determine the spectral parameters i.e. the isomer

shift (IS), the electric quadrupole splitting (QS), the full line width at half maximum (LW) and the relative resonance areas (A) of different components of the absorption patterns (see Appendix A4). The magnetic hyperfine field (H) is absent in the case of these samples confirming the paramagnetic character of the analyzed phases.

Bulk carbon (in inorganic and organic form) and water compositions were determined using step-heating experiments (Javoy and Pineau, 1991; Pineau and Javoy, 1994) at the IPGP (Institut de Physique du Globe de Paris, France) on $\approx$ 100 mg aliquots. First, powders were loaded in a quartz tube connected to a vacuum line and degassed one night at room temperature. A vertical cylindrical furnace (with a temperature stability of $\pm$ 2 °C) was then used to heat progressively the samples at 100 °C for 1 hour to eliminate all surface contaminants e.g., water and other adsorbed compounds. Finally, samples were heated 1 hour at 700 °C and 1 hour at 1100 °C to extract the carbon trapped in the organic and inorganic form respectively. Heating was made under an oxygen atmosphere raised up to 0.4 MPa after 30 min of reaction. Liquid nitrogen was used to cryogenically separate and collect gaseous CO_2 and H_2O. The amount of CO_2 was quantified using a Toepler® pressure gauge with a detection limit of 0.05%. Carbon and water analyses were duplicated to ensure the reproducibility of the data.

3. Results

3.1. Permeability

All reactive percolation experiments displayed a reduction in sample permeability from initial values of $1.6 - 4.6 \times 10^{-15}$ m² (Table 1) down to 0.075×10^{-15} m² (SC1-L), 0.019×10^{-15} m² (SC2-M) and 0.005×10^{-15} m² (SC3-H; Fig. 2). In detail, the way in which permeability decreased varied from one experiment to the other.

The permeability of experiment SC1-L decreased slightly in the early hours of injection ($dk/dt = 1.40 \times 10^{-17}$ m².h^{-1}) before dropping down to 0.08×10^{-15} m² at $t \approx 36$h and declining slightly again until the end of fluid injection ($dk/dt = 6.30 \times 10^{-19}$ m².h^{-1}).

Experiment SC2-M is characterized by four periods of fast permeability drop starting at $t \approx 13$h ($dk/dt = 1.40 \times 10^{-15}$ m².h^{-1}), $t \approx 54$h ($dk/dt = 5.62 \times 10^{-16}$ m².h^{-1}), $t \approx 84$h ($dk/dt = 9.29 \times 10^{-17}$ m².h^{-1}) and $t \approx 107$h ($dk/dt = 2.10 \times 10^{-16}$ m².h^{-1}). These periods were separated by four intervals of low permeability decrease of about 13, 41, 30 and 23 hours, respectively.

339   The permeability of experiment SC3-H is marked by a slow and almost constant decrease

340   of 135 hours ($dk/dt = 1.5 \times 10^{-17}$ m².h^{-1}), then accelerating sharply at $dk/dt = 4.3 \times 10^{-17}$ m².h^{-1}.

341   After 168 hours, the decrease in permeability slowed down to $dk/dt = 1.4 \times 10^{-18}$ m².h^{-1} until

342   the end of injection.

343

344   *3.2. Fluid chemistry*

345

346   The outlet fluids composition at the time of sampling (Fig. 3) denotes the value integrated

347   over the volume of fluids having flowed and reacted with the olivine cores over the 6 hours of

348   reactive percolation experiments preceding sampling (each fluid sample is 3 mL and fluid flux

349   Q is 0.5 mL.h^{-1}). The three experiments were marked by significant changes with time in the

350   outlet fluids composition compared to the injected CO_2-water. First, all outlet fluids displayed

351   enrichments in the three major components of olivine (i.e. Si, Mg and Fe; Fig. 3a,b,c)

352   testifying to the dissolution of the Mg-silicate during the experiments. Second, the sampled

353   outlet fluids were (or became) depleted in Ca indicating the trapping of this element in the

354   percolated cores through the precipitation of Ca-bearing mineral(s) (Fig. 3d). However, the

355   amount of cations released or trapped per time unit varied between the experiments. It should

356   be noted that the outlet fluids sampled at the earliest stages of all experiments (time of

357   sampling < 20h) systematically displayed chemical compositions at odds with the overall

358   chemical trends showed later in the experiments. These variations are controlled by the

359   dissolution of a minor fraction of small grains produced during the preparation of olivine

360   aggregates (Andreani et al., 2009; Godard et al., 2013; Peuble et al., 2015b). These initial

361   processes will not be discussed in details thereafter and we will mainly focus our analysis to *t*

362   > 20h.

363   Experiment SC1-L (lowest concentration in CO_2 = 6.26 mmol.L^{-1}) showed a slight

364   increase in the outlet concentrations of Si (from 43.7 to 62.0 ppm), Mg (from 13.5 to 14.8

365   ppm) and Fe (from 0.2 to 0.7 ppm). But the amount of Mg and Fe is low compared to that of

366   Si and to the olivine stoichiometry; the molar ratios of (Mg/Si)$_{(outlet-inlet)}$ and (Fe/Si)$_{(outlet-inlet)}$ in

367   sampled fluids are 0.15 and 0.01, respectively. This indicates either that the dissolution of

368   olivine was non-stoichiometric or, more probably, that some of the Mg and Fe released upon

369   olivine dissolution remained trapped in the percolated core. The concentrations of Ca, brought

370   in by the inlet fluid, decreased with time from 12.6 to 10.8 ppm in the sampled fluids. This

371   decrease, particularly marked in the first 48 hours of injection (Fig. 3d), suggests that the

372   outlet fluids Ca composition is partly controlled by cation trapping mechanisms. It is worth

noting that the change in chemistry observed in the outlet fluids after 48 hours is close in time to the change in permeability recorded in experiment SC1-L at $t \approx 36$h.

During experiment SC2-M (medium concentration in CO_2 = 62.6 mmol.L^{-1}), Si, Mg and Fe also displayed an increase in their outlet concentrations with time. However, Si concentrations were high (107 to 261 ppm) and their variations erratic (peaks observed at $t \approx$ 13, 83, 134 and 147 hours; Figure 3a) compared to experiment SC1-L. Mg concentrations increased steadily during about 48 hours before stabilizing around 25 ppm. The increase in Fe concentrations followed two plateaus, the first at ≈ 0.3 ppm (from 13 to 109 hours) and the second at ≈ 0.5 ppm (after 122 hours). Compared to experiment SC1-L, Ca concentration values in experiment SC2-M were overall low, decreasing from 12.2 to 9.1 ppm over time. Chemical trends of Si, Mg, Fe and Ca were interpreted as indicating both dissolution of olivine and trapping of Mg, Fe and Ca in the percolated core. Molar ratios of (Mg/Si)$_{(outlet-inlet)}$ and (Fe/Si)$_{(outlet-inlet)}$ were low compared to experiment SC1-L with values of 0.09 and 0.002, respectively; suggesting that the mechanisms controlling the trapping of Mg and Fe were overall more efficient in experiment SC2-M. The irregular and abrupt changes in fluid chemistry during experiment SC2-M also suggest that complex feedback processes between these trapping mechanisms, olivine dissolution and fluid fluxes occurred. For instance, the increase in Mg relative to Si in the first 48 hours suggests that Mg-trapping became less efficient than olivine dissolution yet this period is associated to a strong permeability drop. After 122 hours, the experiment is marked by an increase in Si, Fe and, to a lesser extent, in Ca revealing a further decrease in trapping efficiency while olivine dissolution continued and permeability remained stable.

Compared with experiments SC1-L and SC2-M, the outlet fluids sampled in experiment SC3-H (highest concentration in CO_2 = 659.7 mmol.L^{-1}) are depleted in Fe, but enriched in Mg compared to experiments SC1-L and SC2-M, and in Si compared to experiment SC1-L. Fluid time series are also distinguished by contrasting chemical variations defining two time periods (Fig. 3). The first period, from the start to $t \approx 144$h, is characterized by large changes in the concentrations of all elements: Si concentrations increased rapidly then stabilized at $\approx$ 82 ppm at $t \approx 38$h; Mg concentrations increased sharply at the beginning then slower after $\approx$ 38h before reaching a peak at 64.1 ppm (at $t \approx 70$h) and decreasing down to 38.3 ppm; Fe concentrations were strongly depleted (< 0.03 ppm) except for a peak (up to 0.19 ppm) between 96 and 140 hours; Ca concentrations showed a strong increase during the first hours until a peak (10.5 ppm) was reached at $t \approx 45$h followed by a decrease down to 4.7 ppm (at $t \approx$ 135h). In contrast, the second period, starting after $t \approx 144$h, is characterized by little to no

variations in fluid chemistry. Only Si showed a slow increase up to ≈ 106 ppm and Mg displayed a slight increase at ≈ 45 ppm after 216 hours. Molar ratios of $(Mg/Si)_{(outlet-inlet)}$ and $(Fe/Si)_{(outlet-inlet)}$ were low in the SC3-H sampled fluids (0.54 and 0.0005, respectively) suggesting an efficient trapping of Mg and Fe in the olivine aggregate. However, in contrast to the low pCO_2 experiments, $(Mg/Si)_{(outlet-inlet)}$ changed significantly from 0.70 to 0.43 after t ≈ 144h indicating either a higher release of Si relative to Mg during the dissolution of olivine and/or a more efficient trapping of Mg (together with Ca) during the second period of experiment SC3-H. These chemical changes are associated to variations in rock hydrodynamic properties; the first period is characterized by slow changes in permeability while a significant drop in permeability marks the second period.

3.3. Characterization of the reacted samples

Optical observations shows that the three rock samples remained mainly composed of olivine after the percolation experiments. However, the initial green olivine crystals are covered by a red hue decreasing in intensity away from the inlet (Fig. 4). The red hue coating increases with the CO_2 partial pressure value used in the experiment; it extends to few mm² in sample SC1-L, three-quarters of sample length for sample SC2-M and the whole sample for sample SC3-H.

At the micrometric scale, SEM analyses allow the identification of secondary minerals in the three percolated cores (Fig. 5 and Appendix A1). For the lowest pCO_2 experiments (SC1-L, SC2-M), some pores contain clusters of an amorphous phyllosilicate enriched in Mg ± Fe (Fig. 5a and Appendix A1). Raman analyses suggest that this phase may represent a poorly crystallized precursor of Mg-Fe-rich hydrous minerals such as Fe(III)-rich serpentine (Fig. 6), which is commonly observed in the earliest stages of serpentinization (Andreani et al., 2013). It has Raman peaks comparable to those of lizardite, with a band at 1104 cm^{-1} (Auzende et al., 2004), and those of iddingsite, a Fe(III)-rich olivine alteration product having a non-definite crystal structure, with a first band observed between 611 and 663 cm^{-1} and a second in the O-H bonds spectral region from 3500 to 3600 cm^{-1} (Kuebler, 2013). This alteration product is probably localized at the surface of olivine grains, since olivine peaks are also identified on the Raman spectrum at 824 and 857 cm^{-1} (Cnopnras, 1991). It is associated with hematite showing four Raman bands at 224, 300, 411 and 1322 cm^{-1} (De Faria et al., 1997). Both hydrous phases and iron oxides are found preferentially along the olivine rims located in the vicinity of the inlet; they account for the red hue covering the reacted samples (Fig. 4).

Samples SC1-L and SC2-M contain also micro-grains of silica, Mg-Fe-bearing calcite ($Ca_{0.95}Mg_{0.03}Fe_{0.02}CO_3$) and minor siderite ($Fe_{0.95}Mg_{0.04}Ca_{0.01}CO_3$) that are distributed evenly along the percolated cores (Fig. 5b-c and Appendix A1).

In sample SC3-H, some olivine surfaces exhibit dissolution features forming conical-shaped etch-pits with a maximum length of 1 μm (Fig. 5d-e). Etch-pits are observed along the dissolved olivine surfaces in large pores (10-50 μm) and within the micro-fissures (< 5 μm) that were probably induced by the sample preparation (Peuble et al., 2015a). Sample SC3-H also displays large Mg-carbonate crystals ($Mg_{0.91}Ca_{0.07}Fe_{0.02}CO_3$) forming a matrix of several tens of μm in the pores (Fig. 5f and Appendix A1). This carbonate was identified as magnesite with the typical Raman peak of C-O bonds observed at 1094 cm^{-1} and three minor peaks at 209, 325 and 738 cm^{-1} (Rividi et al., 2010 – see Figure 9). In addition to magnesite, a poorly crystallized phyllosilicate enriched in Fe ± Mg was also characterized in sample SC3-H (Fig. 5d and Appendix A1). This phase forms a dense network of curled fibers similar to the proto-serpentine observed in previous flow-through experiments (Godard et al., 2013). Its Raman spectrum is comparable to the poorly crystallized phase identified in samples SC1-L and SC2-M, forming an assemblage of hydrous minerals and hematite at the olivine grains surface (Fig. 6). The attenuation of the Raman peaks of olivine compared to this proto-serpentine precursor suggests a greater degree of crystallization of the latter in experiment SC3-H than in experiments SC1-L and SC2-M (Kuebler, 2009).

Black grains were observed in pores located close to the inlet in the three reacted samples (< 5 mm - see Figs. 4 and 8). These micron-size grains (<20 μm) were identified as carbon from the D and G bands observed at respective values of 1310 and 1520 cm^{-1} on Raman spectra (e.g., Galvez et al., 2013). Carbon grains have a symmetrical G band in Raman analyses indicative of a poorly ordered crystallographic structure also referred to as turbostratic. Reduced turbostratic carbon or graphene is commonly reported under low temperature conditions i.e. < 400 °C (Audier et al., 1981; Beyssac et al., 2003).

Magnetic susceptibility and Mössbauer analyses were realized on a subset of powders. They show that the precipitation of ferric iron is minimal in the three reacted cores in spite of the change of color observed optically. Samples magnetic susceptibility did not change significantly during reactive percolation experiments suggesting that magnetite did not precipitate during CO_2-fluids injection (see Table 1). Mössbauer measurements identified no ferric iron impurities in the reacted powders in the limit of ≈ 2% (see Fig. 9 and Appendix A4). Note that all Mössbauer spectra were fitted using two doublets (components 1 and 2 corresponding to the M1 and M2 sites of olivine), both having the parameters of high spin

475   Fe^{2+} occupying octahedral sites in the olivine crystals. The isomer shifts and the quadrupole

476   splitting are similar to the reported values for olivine (Dyar et al., 2006). The only differences

477   between these samples are the line widths and the relative fractions of components 1 and 2,

478   which are both within the uncertainty of Mössbauer analyses (i.e. less than $\approx$ 2% relative to

479   the total iron content).

480   Bulk rock hydrogen and carbon analyses indicate that reacted samples were systematically

481   enriched in these two elements relative to the initial olivine (Table 3 and Appendix A5). This

482   is consistent with the presence of secondary hydrous and carbon-bearing phases revealed by

483   the petrological and mineralogical analyses of reacted samples. Bulk powder measurements

484   also show that carbon is present in both inorganic and organic forms in reacted samples SC2-

485   M and SC3-H. Inorganic carbon (carbonates) is dominant after the highest pCO_2 experiment:

486   it represents 97% of the total carbon measured in sample SC3-H. In contrast, inorganic carbon

487   represents only ~ 40% of the measured total carbon in sample SC2-M; the remaining fraction

488   being organic (i.e. reduced) carbon, which suggests less favorable conditions for carbonates

489   precipitation under a lower pCO_2.

490

491   *3.4 Mass estimates of dissolved and precipitated minerals*

492

493   Both olivine and secondary minerals are mainly composed of Si, Mg, Fe and Ca. The

494   mass balance calculation (expressed as oxides mass) of these cations comparing inlet and

495   outlet fluids provides a first insight of the volatile-free bulk mass lost or gained by the

496   ultramafic cores during the experiments (Peuble et al., 2015b). Calculations indicate a total

497   mass loss of 0.22, 1.60 and 2.39% relative to the initial samples mass in experiments SC1-L,

498   SC2-M and SC3-H, respectively (Appendix A6), even though the Ca brought in by fluids is

499   trapped into the samples.

500   Hydrous minerals, oxides and carbonates were identified as secondary phases in the

501   percolated aggregates. Some identified minerals display unreferenced compositions (such as

502   the hydrous phases interpreted as serpentine precursors), albeit they all contain at least Si, Mg,

503   Fe or Ca. Furthermore, bulk analyses could not be used directly to quantify the amount of

504   carbon and hydrogen trapped in reacted samples. First, due to technical problems, hydrogen

505   was not analyzed in one of the samples (sample SC3-H). Second, the distribution of hydrogen

506   and organic and inorganic carbon in sample SC1-L may have been affected by leakage of

507   containment fluid (MilliQ-water in equilibrium with the atmosphere) into the sample Teflon

508   sleeve, when the experiment was stopped ($t \approx$ 93h). For these reasons, the quantification of

dissolved and trapped phases was done only on the basis of fluid time series. In such conditions, estimating the actual mass change of the samples during reactions requires making conjectures on the distribution of cations in secondary minerals (Andreani et al., 2009). For this study, we assume that:

(*i*) The excess of Si measured in the outlet fluids, i.e. $Si_{(outlet-inlet)}$, equals to the Si released by the dissolution of olivine only. In other words, we assumed that the amount of Si trapped in the samples is negligible even if Si-rich secondary phases precipitated in the reacted cores. The calculated mass of dissolved olivine is thus a minimal estimate. Accordingly, we calculated a concentration model of the outlet fluids for Mg and Fe involving the mass of these elements released by olivine dissolution and the mass brought in by the injected fluid. The measured deficits in Mg and Fe relative to this concentration model allow estimating the mass of trapped minerals.

(*ii*) Fe was trapped in carbonates during experiments SC1-L and SC2-M, and Mg was sequestered as magnesite in experiment SC3-H. All Ca was incorporated into carbonates in the three experiments (Fe-bearing calcite in samples SC1-L and SC2-M; Ca-bearing magnesite in sample SC3-H).

(*iii*) The contribution of hydrous silicate minerals associated to (proto-)serpentinization of olivine was approximated from pure end-member components that have been described as 'precursor phases' of serpentine minerals: brucite $(Mg(OH)_2)$ for the Mg(Fe)-rich phyllosilicates in experiments SC1-L and SC2-M (e.g., Ferry, 2000; Tutolo et al., 2018); goethite $(FeO(OH))$ for the Fe(Mg)-rich phyllosilicates in experiment SC3-H (Delvigne et al., 1979; Lee et al., 2015).

The calculated mass of dissolved olivine is 8.34, 63.17 and 62.94 mg in experiments SC1-L, SC2-M and SC3-H, respectively. This represents a mass loss of 0.48, 3.69 and 4.31% relative to the initial mass of samples SC1-L, SC2-M and SC3-H, respectively (Table 4 and Fig. 10). The calculated mass of hydrous Mg-phases in samples SC1-L and SC2-M is 6.82 and 54.08 mg, respectively; this indicates a gain of mass of 0.40 and 3.15% relative to their initial mass, respectively. The calculated mass of hydrous Fe-phases in sample SC3-H is 7.28 mg, corresponding to a relative mass gain of 0.50%. The total mass of carbonates is 1.30, 9.98 and 45.60 mg in samples SC1-L, SC2-M and SC3-H, respectively, representing a relative mass gain of 0.08, 0.58 and 3.12%.

Petrological observations and bulk rock analyses indicated that organic carbon was present in the reacted samples. Bulk rock analyses showed that the carbon content of the initial olivine was below the detection limit, so the only source of carbon is the CO_2-bearing

16

543   injected fluid. In order to evaluate the amount of organic carbon in the three reacted samples,

544   we assumed that (*i*) the measured ratios of organic and inorganic carbon for samples SC3-H

545   and SC2-M were representative of the actual distribution of carbonates versus reduced carbon

546   in the samples, and (*ii*) the ratio of organic and inorganic carbon in sample SC1-L was the

547   same as that of sample SC2-M. Based on the calculated masses of carbonates, the total mass

548   of reduced carbon is 0.19, 1.77 and 0.20 mg in samples SC1-L, SC2-M and SC3-H,

549   respectively and corresponds to a relative mass gain of 0.01, 0.10 and 0.01%, respectively.

550   Based on these calculations, the mass balance between dissolved olivine and precipitated

551   secondary minerals (hydrous phases, reduced carbon and carbonates) led to a negligible total

552   mass change of the cores: a relative mass gain of 0.01 and 0.14% for samples SC1-L and

553   SC2-M, respectively, and a relative mass loss of 0.68% for sample SC3-H. They also indicate

554   that the alteration of olivine into carbon-bearing phases (reduced carbon and carbonates)

555   resulted in a total sequestration of CO_2 of 0.07, 0.60 and 1.66 wt.% in experiments SC1-L,

556   SC2-M and SC3-H, respectively (see Table 4). These values are consistent with bulk rock

557   data measured of samples SC2-M and SC3-H (Fig. 10), which validates a posteriori the

558   assumptions made for the mass balance. Calculations also showed that only 10.5, 4.8 and

559   0.5% of the total amount of CO_2 injected in samples SC1-L, SC2-M and SC3-H respectively,

560   remained trapped as carbon–bearing products (reduced carbon and carbonates). This implies

561   that the percolating fluids were still enriched in CO_2 at the cores outlet.

562

563   *3.5. Porosity variation during olivine alteration*

564

565   Changes in rock porosity induced by the percolation of CO_2-fluids in the ultramafic cores

566   can be inferred from the calculated mineral masses. A volumetric mass density of 3.3 g.cm^{-3}

567   was assumed for olivine (Deer et al., 1992). The total volume of carbonates was assessed from

568   the volumetric mass density of calcite ($\rho_{calcite}$ = 2.7 g.cm^{-3}) and siderite ($\rho_{siderite}$ = 3.9 g.cm^{-3}

569   ) in experiments SC1-L and SC2-M, and of magnesite ($\rho_{magnesite}$ = 3.0 g.cm^{-3}) in

570   experiment SC3-H (Deer et al., 1992). Two end-member scenarios were used to estimate the

571   volume of hydrous phases considering the density of their expected precursors (brucite in

572   samples SC1-L and SC2-M ($\rho_{brucite}$ = 2.4 g.cm^{-3}); goethite in sample SC3-H ($\rho_{goethite}$ = 4.3

573   g.cm^{-3})) or that of lizardite as a serpentine-type mineral ($\rho_{lizardite}$ = 2.6 g.cm^{-3}) (Deer et al.,

574   1992). The precipitation of reduced carbon was considered as negligible.

575   Results show that changes in porosity are relatively small during the percolation
576   experiments (Table 4, Fig. 10c and Appendix A7). Samples porosity was reduced from
577   10.96% to 10.80% in experiment SC1-L and from 11.30% to 9.89% in experiment SC2-M
578   according to the different scenarios of carbonate formation (calcite or siderite) and hydration
579   (brucite or lizardite). Compared to the initial samples porosity, these results correspond to a
580   maximum porosity change of ~1% and ~12% in experiments SC1-L and SC2-M, respectively.
581   In experiment SC3-H, the porosity increased by ~5% (from 10.57 to 11.11%) or ~3% (from
582   10.57 to 10.86%) considering the precipitation of magnesite and goethite or the precipitation
583   of magnesite and lizardite, respectively.

584

585   **4. Discussion**

586

587   All reacted samples show the alteration of olivine into secondary minerals. However, the
588   nature and rate of dissolution and precipitation reactions are variable depending on the inlet
589   fluid pCO_2. The experiments with the lowest pCO_2 (0.1 – 1 MPa i.e. CO_2 = 6.26 – 62.6
590   mmol.L^{-1}) are characterized by the formation of Mg(Fe)-rich phyllosilicates associated with
591   Ca- and Fe-carbonates. The high pCO_2 experiment (10 MPa i.e. CO_2 = 659.7 mmol.L^{-1})
592   involves the precipitation of magnesite and Fe(Mg)-rich phyllosilicates. All percolated cores
593   contain hematite and reduced carbon. Hereafter, we will discuss the role of CO_2 on the
594   hydrothermal alteration of olivine and the fate of carbon in the ultramafic aggregates.

595

596   *4.1. Alteration of olivine and formation of carbonates during low CO_2 concentration*
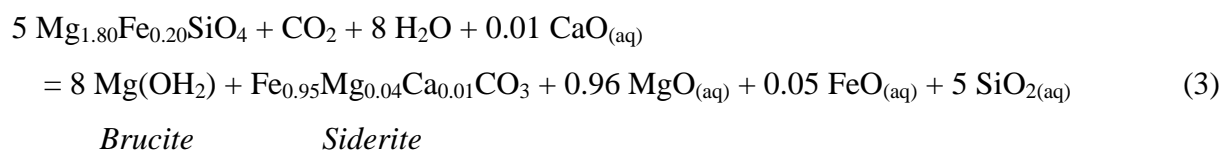597   *experiments (6.26 – 62.6 mmol.L^{-1})*

598

599   The comparison of experiments SC1-L and SC2-M shows an increase in the mean
600   dissolution rate of olivine with CO_2 partial pressure: 1.43×10^{-8} s^{-1} at pCO_2 = 0.1 MPa
601   (sample SC1-L); 6.55×10^{-8} s^{-1} at pCO_2 = 1 MPa (sample SC2-M). These results are
602   consistent with previous studies reporting the effect of CO_2 concentration on olivine
603   dissolution rates by controlling the activity of H$^+$ ions in the solution (Rosso and Rimstidt,
604   2000; Hänchen et al., 2006). H$^+$ ions are assumed to govern the kinetics of olivine dissolution
605   by favoring the protonation of Mg–O and Fe–O bonds (in Mg–O–Si and Fe–O–Si
606   arrangements) to form Mg and Fe complexes associated with silicic acid (Casey and Bunker,
607   1990; Wogelius and Walther, 1990; Pokrovsky and Schott, 2000). In our study, the
608   dissolution rate of olivine is correlated to the activity of protons in the fluid: it is multiplied by

609　4.6 when the H$^+$ concentration is quadrupled between experiments SC1-L (H$^+$ = 0.04 mmol.L$^-$

610　^{1}) and SC2-M (H$^+$ = 0.16 mmol.L^{-1}) based on PhreeqC calculations (Parkhurst and Appelo,

611　2013). However, the outlet concentrations of Si showed that the dissolution rate of olivine

612　evolved differently between these two experiments: it reached rapidly a steady state in

613　experiment SC1-L while it fluctuated throughout experiment SC2-M.

614　　　In porous media, the dissolution rate of olivine is controlled by local chemical equilibrium

615　conditions, which are themselves determined by the mass transfer of solutes to reactive sites,

616　the adsorption of such chemical species at the Mg-silicate surface and the residence time of

617　fluids at mineral interfaces (Peuble et al., 2015b). Accordingly, we postulate that the injection

618　of a low concentration of H$^+$ ions in experiment SC1-L (pCO_2 = 0.1 MPa) allowed the

619　dissolution rate of olivine to rapidly achieve a steady state at the sample scale, independently

620　of the rock hydrodynamic properties. In experiment SC2-M, CO_2 concentrations were 10

621　times greater (pCO_2 = 1 MPa), which increased the difference to equilibrium between olivine

622　and fluids. During this experiment, the olivine dissolution rate never reached a steady state.

623　We speculate that this rate varied locally and temporally along the percolated core depending

624　on local fluid flow conditions and reactive surface areas.

625　　　Unlike the dissolution of olivine, the outlet concentrations of Ca and Fe suggest that the

626　precipitation rate of Ca-carbonates and Fe-bearing phases (carbonates and oxides) reached a

627　steady state in both low pCO_2 experiments (except for Fe in sample SC1-L). The precipitation

628　of Ca- and Fe- carbonates (i.e. calcite and siderite) appears contradictory with the Mg-rich

629　composition of the initial ultramafic system (olivine Fo$_{90}$). Furthermore, the outlet fluids of

630　low pCO_2 experiments do contain magnesium coming from the dissolution of olivine (Fig.

631　3b), and PhreeqC geochemical simulations indicate that they are supersaturated with respect

632　to magnesite (Parkhurst and Appelo, 2013). These inconsistencies highlight the competitive

633　processes in the precipitation kinetics between Mg-, Ca- and Fe-carbonates, due to the

634　different chemical affinities of Mg^{2+}, Ca^{2+} and Fe^{2+} ions with water (e.g., Pokrovsky and

635　Schott, 2002). Mg^{2+} has a highly hydrated character compared to Ca^{2+} and Fe^{2+} (Pokrovsky

636　and Schott, 2002; Schott et al., 2009; Gautier, 2012). Hänchen et al. (2008) observed that the

637　crystallization of magnesite is generally hindered by the intermediate precipitation of hydrous

638　Mg-carbonates (e.g., nesquehonite, hydromagnesite) especially under low CO_2 partial

639　pressure conditions (< 0.3 MPa). Hence, the precipitation rate of magnesite can be up to six

640　orders of magnitude slower than that of other carbonates such as calcite (Saldi et al., 2009;

641　Saldi et al., 2012). Because of these thermo-kinetic restrictions, the Mg-rich samples SC1-L

642　and SC2-M promoted the crystallization of calcite and siderite at the expense of magnesite.

643   This means that the potential for CO_2 mineralization in olivine-dominated basements under

644   low pCO_2 conditions ($0.1 - 1$ MPa) is primarily regulated by the amount of iron provided by

645   the mafic silicate and the amount of calcium brought in by the percolating fluids; both

646   mechanisms favoring the precipitation of siderite ± calcite. Magnesium is mainly incorporated

647   into transient, hydrous and amorphous phases (Mg(Fe)-rich (proto-)phyllosilicates) that

648   probably developed from the destabilization of brucite, as it is commonly reported during

649   serpentinization of olivine (Delvigne et al., 1979; Escario et al., 2018; Tutolo et al., 2018).

650   Thus, if we tentatively extrapolate these results to ultramafic reservoirs infiltrated by

651   relatively low pCO_2 waters, we can model the hydrothermal alteration of olivine in areas

652   located far from the CO_2 input by the following reaction:

653

654    $5\ Mg_{1.80}Fe_{0.20}SiO_4 + CO_2 + 8\ H_2O + 0.01\ CaO_{(aq)}$

655       $= 8\ Mg(OH_2) + Fe_{0.95}Mg_{0.04}Ca_{0.01}CO_3 + 0.96\ MgO_{(aq)} + 0.05\ FeO_{(aq)} + 5\ SiO_{2(aq)}$ (3)

656   *Brucite*   *Siderite*

657

658   Under low CO_2 concentrations (here defined as being ≤ 62.6 mmol.L^{-1}), the dissolution of

659   five moles of olivine produces eight moles of hydrous minerals (e.g., brucite) but only one

660   mole of Fe-carbonates. Such olivine alteration products (especially brucite) may then induce

661   negative feedback effects on the completion of the reaction (Malvoisin and Brunet, 2014), but

662   also on the hydrodynamic properties of the rock. Indeed, differential pressure measurements

663   revealed a sharp decrease in the permeability of samples SC1-L and SC2-M even though

664   porosity values display little change over time. This suggests that the decrease in permeability

665   is primarily controlled by the structure of secondary minerals (mainly the hydrous phases)

666   clogging fluid pathways in the host rock, in agreement with the results obtained in previous

667   flow-through serpentinization experiments for similar fluid flow conditions (Godard et al.,

668   2013; Peuble et al., 2015b; Farough et al., 2016; Luhmann et al., 2017a).
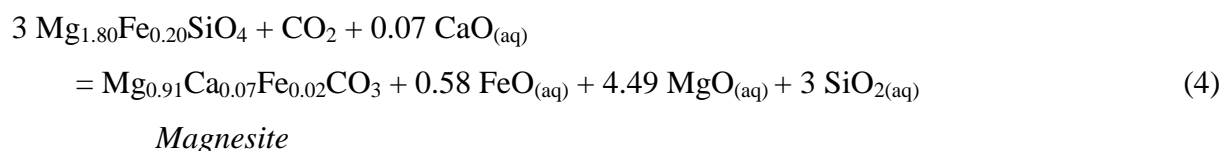
669

670   *4.2. Alteration of olivine and formation of carbonates during a high CO_2 concentration*

671   *experiment (659.7 mmol.L^{-1})*

672

673   High pCO_2 experiment SC3-H has probably the highest dissolution rate of olivine, and

674   paradoxically, lower Si outlet fluid concentrations than in experiment SC2-M. The strong

675   dissolution of olivine in sample SC3-H is characterized by abundant etch-pits, similar to those

676   described on several experimental (e.g., Grandstaff, 1978; Malvoisin et al., 2012; King et al.,

677　2014; Peuble et al., 2015a) and natural samples (Velbel and Ranck, 2008; Velbel, 2009), and

678　attributed to an anisotropic dissolution of the Mg-silicate (King et al., 2014; Peuble et al.,

679　2015a). The relatively low concentrations of Si in this experiment can be ascribed to the

680　development of large Fe(Mg)-rich phyllosilicates (Fig. 5d), trapping part of the Si released

681　upon olivine dissolution. As for the hydrous minerals of low pCO_2 experiments, these

682　phyllosilicates are presumably transitional phases formed before serpentinization. However,

683　their formation appears to be related to the pCO_2 since the largest phyllosilicates were

684　observed in sample SC3-H. We postulate that the use of a higher concentration of CO_2 in this

685　experiment has facilitated the growth of these phases by increasing the dissolution rate of

686　olivine under lower pH conditions (Wogelius and Walther, 1990; Hänchen et al., 2006;

687　Prigiobbe et al., 2009).

688　　　The identified serpentine precursors resemble an iddingsitized form of olivine according

689　to optical, microscopic and Raman observations (Figs. 4-6). Iddingsitization of olivine is an

690　oxidation and hydration reaction leading to the conservation of Si, the loss of Mg (that is

691　leached out from the olivine surfaces) and the gain of Fe (being preferentially converted into

692　ferric iron) in weathered ultramafic rocks (Delvigne et al., 1979). The more prominent

693　serpentine precursors in sample SC3-H (compared to samples SC1-L and SC2-M) have

694　depleted the percolating fluids in Si and Fe relative to Mg suggesting an underestimation of

695　the olivine dissolution rate in sample SC3-H (compared to samples SC1-L and SC2-M). They

696　also promoted the concentration of ferric iron micro-particles (hematite) along dissolved

697　olivine surfaces. These Fe-oxides may then have acted as preferential nuclei for the

698　polymerization of Fe(Mg)-rich phyllosilicates, as it was previously observed during late

699　stages of olivine iddingsitization (Lee et al., 2015).

700　　　In sample SC3-H, most of the Mg released upon olivine dissolution was incorporated into

701　a large matrix of magnesite (Fig. 5f). These results confirm that a high concentration of CO_2

702　(659.7 $mmol.L^{-1}$), resulting in a high dissolution rate of olivine and consequently a high

703　concentration of Mg^{2+} in the fluid, is required to overcome the difficulty of Mg-carbonates

704　precipitation (due to the highly hydrated character of Mg^{2+} compared with Ca^{2+} and Fe^{2+} ions

705　- see discussion before). Under these conditions, the main alteration reaction of olivine is

706　dominated by the formation of magnesite according to the following reaction:

707

708　$3\ Mg_{1.80}Fe_{0.20}SiO_4 + CO_2 + 0.07\ CaO_{(aq)}$

709　　　$= Mg_{0.91}Ca_{0.07}Fe_{0.02}CO_3 + 0.58\ FeO_{(aq)} + 4.49\ MgO_{(aq)} + 3\ SiO_{2(aq)}$　　　　　　(4)

710　　　　*Magnesite*

712   The comparison of reactions (3) and (4) shows that, for every mole of CO_2 converted into

713   carbonates, five moles of olivine need to be dissolved in the low pCO_2 experiments but only

714   three in the high pCO_2 experiment. This demonstrates a greater potential of olivine to trap

715   CO_2 as carbonates when the inlet fluid has a higher partial pressure of CO_2.

716   Magnesite is associated with Fe(Mg)-rich phyllosilicates in sample SC3-H. However, the

717   outlet concentration values of Mg, Fe and Ca indicate that these two secondary minerals

718   precipitated at different times in the ultramafic core. The sharp decrease in Fe outlet

719   concentrations coupled with the increasing release of Mg in the first hours of injection suggest

720   an almost immediate polymerization of serpentine fibrous precursors. This process then

721   slowed down after 84 hours, with the increase in Fe outlet concentrations up to ≈ 0.19 ppm.

722   At $t \approx 45h$, magnesite began to crystallize by first incorporating calcium, then magnesium and

723   iron, resulting in a significant decrease in the outlet concentrations of Ca, Mg and Fe after $t \approx$

724   45, 71 and 116 hours, respectively. These concentrations stabilized after 135 hours, indicating

725   that the olivine carbonation rate rapidly reached a steady state in the percolated aggregate.

726   The onset of the stable carbonation of olivine is correlated with a linear decrease in

727   permeability after 135 hours in sample SC3-H. As in low pCO_2 experiments, this correlation

728   attests to negative feedback effects of some olivine alteration products on rock flow paths by

729   reducing pore hydraulic radius and increasing pore tortuosity over time. However, the

730   porosity of sample SC3-H increased throughout the injection whatever the scenarios

731   considered (Fig. 10c). These results suggest first that the overall decrease in rock pore volume

732   during magnesite and serpentine precursors precipitation is (at least temporarily and locally)

733   offset by the porosity created upon olivine dissolution, maintaining fluid renewal at reaction

734   front interfaces (Peuble et al., 2017). They also show that the decrease in permeability

735   recorded during experiment SC3-H is not controlled by the crystallization of secondary

736   minerals. The decrease in permeability is most likely attributed to the heterogeneous

737   distribution of these secondary minerals in the percolated core, which affects primarily the

738   major fluid pathways.

739

740   *4.3. Oxidation of olivine ferrous iron and the fate of carbon*

741

742   The characterization of reacted samples revealed the presence of reduced carbon, trapping

743   from 0.04% (sample SC3-H) to 0.17% (sample SC2-M) of the CO_2 injected into the

744   percolated olivine aggregates (Fig. 8 and Table 3). To our knowledge, it is the first time that

745 reduced carbon was measured after olivine alteration experiments in presence of CO_2-bearing
746 fluids although it is observed in oceanic and ophiolitic serpentinites (Ménez et al., 2012;
747 Galvez et al., 2013; Sforna et al., 2018), sometimes in association to carbonates
748 (Schwarzenbach et al., 2016). Also, it is worth to note that the precipitation of reduced carbon
749 has been previously reported after another set of reactive percolation experiments using a
750 different set-up and flow-bench (Luquot et al., 2012). These reactive percolation experiments
751 consisted in injecting of CO_2-bearing brines (pCO_2 = 6 MPa; CO_2 = 402 mmol.L^{-1}) into
752 chlorite/zeolite-rich sandstones at T=95 °C and P=10 MPa. They produced reduced carbon
753 grains with the same poorly organized crystallographic structure as those observed in our
754 samples. Luquot et al. (2012) proposed that these carbon grains were formed after
755 concomitant reduction of the injected CO_2 in association to the oxidation of ferrous iron in
756 chlorite. The oxidation of iron liberates electrons (Eq. 5), inducing locally a more reduced
757 environment, which in turn would favor carbon reduction (Eq. 6).

758 $Fe^{2+} = Fe^{3+} + e^-$ $\hspace{6cm}$ (5)

759 $CO_2 + 4H^+ + 4 e^- = C^0 + 2H_2O$ $\hspace{5cm}$ (6)

760 The oxidation of Fe^{2+} during serpentinization is often associated to the abiotic generation
761 of H_2 produced from H_2O reduction. Subsequently, H_2 can react with CO_2 to form a wide
762 range of reduced carbon species including condensed carbonaceous matter (Galvez et al.,
763 2013; Martinez et al., 2017; Sforna et al., 2018) and possibly methane (McCollom, 2016).
764 Some studies have shown that the production of reduced carbon-bearing phases may be
765 kinetically favored in serpentinizing ultramafic systems when metal alloys are present (Horita
766 and Berndt, 1999; Fu et al., 2008; Lazar et al., 2012) because they act as catalysts.
767 Accordingly, we can question the fact that the sintered nickel porous disk positionned
768 upstream of the olivine sample can have acted similarly during our experiments thus favoring
769 the formation of reduced carbon phases albeit, to our knowledge, Ni-Fe alloys have been
770 shown to act as catalysts of the methane production only (Horita and Berndt, 1999).
771 Alternatively, Milesi et al. (2016) recently demonstrated on the basis of thermodynamical
772 calculations that solid carbonaceous material can be formed during serpentinization without
773 catalysts. Furthermore, they showed that the compositions of fluids sampled in ultramafic-
774 hosted hydrothermal vents were consistent with an equilibrium between $CO_{2(aq)}$ and some
775 condensed carbon phases, thus suggesting that these reactions are probably of major
776 importance in ultramafic basements along oceanic spreading centers.

777 During our experiments, the presence of hematite and iddingsite at the olivine surface
778 indicates that oxidation of ferrous iron did occur at the fluid/mineral interface. The pH and pE

of the inlet fluids were calculated using the PhreeqC geochemical code (Parkhurst and Appelo, 2013); pH values of 4.5, 3.9 and 3.4 and pE values of 5.4, 6.5 and 7.3 were estimated for experiments SC1-L, SC2-M and SC3-H, respectively. When reported on a pE-pH stability diagram of Fe- and C-species, hematite is thermodynamically stable for the conditions characterizing the inlet fluid, which is consistent with a reaction of Fe^{2+} oxidation at the sample inlet (Figure 11a, b, and c). This oxidation reaction is probably balanced by the reduction of CO_2 into carbon, promoting a strong decrease in the fluid pE down to -2.6, -1.4 and -0.3 in experiments SC1-L, SC2-M and SC3-H, respectively. So, assuming that pH stays low and constant (e.g., at the onset of the reaction or close to the CO_2 injection point), carbon reduction could be favored over water reduction (and hydrogen production) (Figure 11d, e, and f), in contrast to what is classically suggested in the literature to balance the oxidation of ferrous iron during serpentinization (Klein et al., 2009). However, the field of stability of carbon is very narrow and olivine dissolution will increase the pH of reacting fluids downstream, consuming H^+ ions in the solutions (Pokrovsky and Schott, 2000; Escario et al., 2018). The observation of carbonates in samples SC1-L, SC2-M and SC3-H suggests an increase of the fluid pH to at least values of 6.3, 5.4 and 4.8, respectively. The precipitation of hydrous phases (Fe(Mg)-rich phyllosilicates) requires an increase of pH to at least values of 6.6 in experiments SC1-L – SC2-M and of 7.5 in experiment SC3-H (Fig. 11a-c). This two-step mechanism (redox reactions followed by dissolution-precipitation reactions), by which reactions along flow paths are controlled by feedback processes between the dissolution of olivine and the changes in fluid composition (including pH), could explain both the limited distribution of reduced carbon, observed only in the pores close to the inlet (Fig. 8), and the predominance of carbonate and hydrous phases in the reacted samples. It is worth noticing that carbonate (magnesite) precipitation conditions are favored in the high pCO_2 experiment (minimum pE-pH variations), which could explain the observed high carbonation efficiency in sample SC3-H.

Thermodynamic modeling suggests that carbon reduction is strongly controlled by the low pH of fluids, a condition that is rarely met in natural carbonate bearing serpentinizing ultramafic basements, which are dominated by alkaline fluids (Ludwig et al., 2006; Chavagnac et al., 2013; Milesi et al., 2016). This process should however be taken into account when predicting the fate of carbon in the case of a CO_2-injection experiment in an ultramafic basement.

5. Summary and conclusions

813

814   This experimental study explores the role of CO_2 and fluid flow on the hydrothermal

815   alteration of olivine. Results provide new information to characterize the fluid-rock reactions

816   in the case of an ultramafic aquifer pervaded by CO_2-rich hydrothermal waters. It is the first

817   step to improve the parameterization of future numerical models specifically by allowing the

818   measurement of macroscopic characteristics of the mass transfer mechanisms resulting from

819   complex coupled flow-reaction pore scale processes.

820   Far from the CO_2 input i.e. under low pCO_2 conditions (from 0.1 to 1 MPa), olivine will

821   be mainly altered into hematite and Mg(Fe)-rich phyllosilicates. These iddingsitic-type

822   assemblages may clog most of the rock flow paths, resulting in a strong decrease in

823   permeability in a few days. Some carbonates can form in these conditions, but they are mainly

824   composed of calcium and iron despite the initial Mg-rich system (Fo_{90}). This denotes less

825   favorable conditions of crystallization for Mg- than for Ca- and Fe-carbonates.

826   Closer to the CO_2 input (i.e. pCO_2 = 10 MPa), olivine will be more efficiently altered.

827   This causes the formation of abundant etch-pits on the olivine surfaces and a larger amount of

828   poorly crystallized Fe(Mg)-rich phyllosilicates depleting the percolating fluids in Si and Fe

829   relative to Mg. In addition to these hydrous phases, magnesite precipitates as dense clusters in

830   the large pores. The carbonation rate of olivine can be 3 to 11 times higher at a pCO_2 of 10

831   MPa than when pCO_2 is 10 to 100 times lower, respectively. Both carbonated and hydrous

832   minerals induce apparently little changes in porosity but a strong decrease in permeability,

833   attesting to negative feedback effects of the olivine alteration products on the fluid flow.

834   Despite the differences in secondary mineralogy between the low and high pCO_2

835   experiments, all samples contain reduced carbon that may indicate a competition for reduction

836   and carbonation processes; both participating to the mineral sequestration of CO_2. Carbon

837   formation suggests reducing conditions probably caused by the oxidation of ferrous iron into

838   ferric iron. For the specific boundary condition of the experiments, carbon deposits are limited

839   to the pores located at the inlet in relation to the low production of hematite and the pH

840   gradient in the samples. Nevertheless, one can speculate that the formation of carbon can be a

841   significant mechanism of CO_2 sequestration in olivine-dominated basements.

842   For industrial application, long lasting injection is required. Accordingly, the objective

843   should be to prevent as best as possible precipitation in the vicinity of the well and to favor

844   mineralization as far as possible from the injection well. When investigating the injection of a

845   reactive fluid from a well, the most important feature is that seepage velocity decreases

846   linearly to quadratically as the distance to injection increases and therefore the apparent (or

847 dynamic) water/rock ratio decreases rapidly. Consequently, the most important feature for

848 optimizing injection is to inject at the largest flow rate as possible in order to locate

849 mineralization as far as possible from the injection well and thus mitigate permeability

850 reduction effects. From this perspective, one can speculate from the permeability (Fig. 2) and

851 CO_2 trapping (Fig. 10) curves that the medium pCO_2 value (1 MPa) would be the most

852 favorable option.

853

862
863
864 **Table captions**

865

866 Table 1. Experimental setup and sample characteristics for the three experiments.

867

868 Table 2. Concentrations of major elements (Si, Mg, Fe and Ca, in ppm) measured in the inlet

869 fluid by ICP-MS.

870

871 Table 3. Bulk rock analyses. Hydrogen and carbon contents recalculated as H_2O and CO_2

872 contents respectively in the initial powder and the percolated olivine cores SC2-M and SC3-H

873 (analytical blanks subtracted).

874

875 Table 4. Mass balance calculations. Estimates of dissolved olivine and precipitated secondary

876 minerals relative to the initial samples mass, and corresponding changes in rock porosity.

877

878 **Figure captions**

879

880 Figure 1. Diagram of the ICARE-RFTS3 experimental device (Geosciences Montpellier).

881

882 Figure 2. Samples permeability k (in 10^{-15} m²) as a function of time (in hours) during

883 experiments SC1-L ($pCO_2 = 0.1$ MPa; $CO_2 = 6.26$ mmol.L^{-1}), SC2-M ($pCO_2 = 1$ MPa; $CO_2 =$

884 62.6 mmol.L^{-1}) and SC3-H ($pCO_2 = 10$ MPa; $CO_2 = 659.7$ mmol.L^{-1}). Symbols in inset.

885

886 Figure 3. (a) Si, (b) Mg, (c) Fe and (d) Ca outlet fluid concentrations (in ppm) versus the

887 elapsed time of the experiments (in hours). Dotted lines correspond to the inlet fluid

888 composition. Symbols in inset.

889

890 Figure 4. Binocular microscope photography of the olivine aggregates (a) before and (b,c,d)

891 after the percolation experiments: (b) sample SC1-L ($pCO_2 = 0.1$ MPa; $CO_2 = 6.26$ mmol.L^{-}

892 ^{1}), (c) sample SC2-M ($pCO_2 = 1$ MPa; $CO_2 = 62.6$ mmol.L^{-1}) and (d) sample SC3-H ($pCO_2 =$

893 10 MPa; $CO_2 = 659.7$ mmol.L^{-1}). White arrows denote the fluid flow direction during the

894 experiments. The white square indicates the location of the SEM image displayed in Figure 8.

895

896 Figure 5. SEM images of the samples after the experiments (a,b) SC1-L ($pCO_2 = 0.1$ MPa;

897 $CO_2 = 6.26$ mmol.L^{-1}), (c) SC2-M ($pCO_2 = 1$ MPa; $CO_2 = 62.6$ mmol.L^{-1}) and (d,e,f) SC3-H

898 ($pCO_2 = 10$ MPa; $CO_2 = 659.7$ mmol.L^{-1}). Reacted samples are mainly composed of olivine.

899 (a,b,c) Formation of amorphous Mg(Fe)-rich phyllosilicates (phyll) associated with

900 micrograins of silica, calcite and siderite. (d) Precipitation of poorly crystallized Fe(Mg)-rich

901 phyllosilicates forming a loose network of curled fibers. (e) Strong dissolution of olivine

902 evidenced by the development of conical-shaped etch-pits. (f) Sample SC3-H is also

903 characterized by the formation of dense clusters of magnesite (mgn) in large pores located

904 near dissolved olivine grains.

905

906 Figure 6. Raman analyses performed in the inlet area (< 5 mm) of the three percolated

907 samples. Raman spectra of forsterite, hematite, lizardite and iddingsite are from Cnopnras et

908 al. (1991), De Faria et al. (1997), Auzende et al. (2004), and Kuebler et al. (2003),

909 respectively.

910

911 Figure 7. Raman spectrum of the percolated sample SC3-H ($pCO_2 = 10$ MPa; $CO_2 = 659.7$

912 mmol.L^{-1}). The standard spectrum of magnesite is shown for comparison (Rividi et al., 2010).

913

914 Figure 8. (a, b) SEM images showing organic carbon in pores located at the inlet (< 5 mm). in
915 sample SC2-M (pCO_2 = 1 MPa; CO_2 = 62.6 mmol.L^{-1}). (c) Raman spectrum obtained on the
916 corresponding area with the typical D and G bands of reduced carbon at respective values of
917 1310 and 1560 cm^{-1} (Galvez et al., 2013).

918

919 Figure 9. Room temperature Mössbauer spectra performed on (a) the initial bulk rock and the
920 reacted powders of (b) sample SC1-L (pCO_2 = 0.1 MPa; CO_2 = 6.26 mmol.L^{-1}), (c) sample
921 SC2-M (pCO_2 = 1 MPa; CO_2 = 62.6 mmol.L^{-1}) and (d) sample SC3-H (pCO_2 = 10 MPa; CO_2
922 = 659.7 mmol.L^{-1}). The experimental data are represented with circles, the fitted components
923 with dotted light and dark grey lines. Symbols in inset.

924

925 Figure 10: Mass (a) of dissolved olivine and (b) CO_2 trapped as carbon and carbonates
926 normalized to the initial samples mass. CO_2 contents deduced from geochemical analyses are
927 also reported. (c) Changes in porosity induced by the alteration of olivine into carbonates
928 (siderite or calcite in samples SC1-L and SC2-M; magnesite in sample SC3-H) and hydrous
929 phases (brucite or lizardite in samples SC1-L and SC2-M; goethite or lizardite in sample SC3-
930 H) in relation to the initial samples porosity. See text for details. Symbols in inset.

931

932 Figure 11: pH-pE stability diagram of (a, b, c) iron and (d, e, f) carbon phases . Calculations
933 are made at 185 °C under the CO_2 concentration conditions of (a, d) experiment SC1-L (CO_2
934 = 6.26 mmol.L^{-1}), (b, e) experiment SC2-M (CO_2 = 62.6 mmol.L^{-1}) and (c, f) experiment
935 SC3-H (CO_2 = 659.7 mmol.L^{-1}) using the JCHESS geochemical code (Van Der Lee and De
936 Windt, 2001). Crosses represent the initial pE and pH conditions of the fluid in each
937 experiment according to the calculations made with the PhreeqC geochemical code (Parkhurst
938 and Appelo, 2013). Initial pE values were calculated assuming an electric potential of -0.3 for
939 a Volvic® water at 25 °C and 0.1 MPa (Lorne et al., 1999). Abbreviations: mgt: magnetite;
940 Fe-phyll: Fe-rich phyllosilicates, sid: siderite.

941
942
943 **References**

944

945 Andreani, M., Luquot, L., Gouze, P., Godard, M., Hoise, E., Gibert, B., 2009. Experimental
946 study of carbon sequestration reactions controlled by the percolation of CO_2-rich brine
947 through peridotites. Environmental Science & Technology 43, 1226-1231.

948 Andreani, M., Mevel, C., Boullier, A.M., Escartin, J., 2007. Dynamic control on serpentine
949 crystallization in veins: constraints on hydration processes in oceanic peridotites.
950 Geochemistry Geophysics Geosystems 8, 1-24.

951 Andreani, M., Munoz, M., Marcaillou, C., Delacour, A., 2013. µXANES study of iron redox
952 state in serpentine during oceanic serpentinization. Lithos 178, 70-83.

953 Audier, M., Oberlin, A., Oberlin, M., Coulon, M., Bonnetain, L., 1981. Morphology and
954 crystalline order in catalytic carbons. Carbon 19, 217-224.

955 Auzende, A.-L., Daniel, I., Reynard, B., Lemaire, C., Guyot, F., 2004. High-pressure
956 behaviour of serpentine minerals: a Raman spectroscopic study. Physics and Chemistry of
957 Minerals 31, 269-277.

958 Bearat, H., McKelvy, M.J., Chizmeshya, A.V.G., Gormley, D., Nunuez, R., Carpenter, R.W.,
959 Squires, K., Wolf, G.H., 2006. Carbon sequestration via aqueous olivine mineral carbonation:
960 role of passivating layer formation. Environmental Science & Technology 40, 4802-4808.

961 Bernoulli, D., Weissert, H., 1985. Sedimentary fabrics in Alpine ophicalcites, south Pennine
962 Arosa zone, Switzerland. Geology 13, 755-758.

963 Beyssac, O., Goffe, B., Petitet, J.-P., Froigneux, E., Moreau, M., Rouzaud, J.-N., 2003. On the
964 characterization of disordered and heterogeneous carbonaceous materials by Raman
965 spectroscopy. Spectrochimica Acta Part A 59, 2267-2276.

966 Casey, W.H., Bunker, B., 1990. Leaching of mineral and glass surfaces during dissolution.
967 Reviews in mineralogy and geochemistry 23, 397-426.

968 Chavagnac, V., Monnin, C., Ceuleneer, G., Boulart, C., Hoareau, G., 2013. Characterization
969 of hyperalkaline fluids produced by low‐temperature serpentinization of mantle peridotites
970 in the Oman and Ligurian ophiolites. Geochemistry, Geophysics, Geosystems 14, 2496-2522.

971 Cnopnras, A., 1991. Single crystal Raman spectra of forsterite, fayalite, and monticellite.
972 American Mineralogist 76, 110L1109.

973 Coggon, R.M., Teagle, D.A.H., Smith-Duque, C.E., Alt, J.C., Cooper, M.J., 2010.
974 Reconstructing past seawater Mg/Ca and Sr/Ca from mid-ocean ridge flank calcium carbonate
975 veins. Science 327, 1114-1117.

976 Dasgupta, R., Hirschmann, M.M., 2010. The deep carbon cycle and melting in Earth's
977 interior. Earth and Planetary Science Letters 298, 1-13.

978 Daval, D., Hellmann, R., Saldi, G.D., Wirth, R., Knauss, K.G., 2013. Linking nm-scale
979 measurements of the anisotropy of silicate surface reactivity to macroscopic dissolution rate
980 laws: New insights based on diopside. Geochimica et Cosmochimica Acta 107, 121-134.

981 Daval, D., Sissmann, O., Menguy, N., Saldi, G.D., Guyot, F., Martinez, I., Corvisier, J., 982 Garcia, B., Machouk, I., Knauss, K.G., Hellmann, R., 2011. Influence of amorphous silica 983 layer formation on the dissolution rate of olivine at 90°C and elevated pCO_2. Chemical 984 Geology 284, 193-209.

985 De Faria, D.L.A., Venâncio Silva, S., De Oliveira, M.T., 1997. Raman microspectroscopy of 986 some iron oxides and oxyhydroxides. Journal of Raman spectroscopy 28, 873-878.

987 Deer, W.A., Howie, R.A., Zussman, J., 1992. An introduction to the rock-forming minerals. 988 Longman Scientific & Technical Hong Kong.

989 Delvigne, J., Bisdom, E.B.A., Sleeman, J., Stoops, G., 1979. Olivines, their pseudomorphs 990 and secondary products. Stiboka.

991 Dullien, F.A.L., 1979. Porous media: fluid transport and pore structure. Academic press, 992 New-York.

993 Dyar, M.D., Agresti, D.G., Schaefer, M.W., Grant, C.A., Sklute, E.C., 2006. Mössbauer 994 Spectroscopy of Earth and Planetary Materials. Annual Review of Earth and Planetary 995 Sciences 34, 83-125.

996 Escario, S., Godard, M., Gouze, P., Leprovost, R., 2018. Experimental study of the effects of 997 solute transport on reaction paths during incipient serpentinization. Lithos.

998 Farough, A., Moore, D.E., Lockner, D.A., Lowell, R.P., 2016. Evolution of fracture 999 permeability of ultramafic rocks undergoing serpentinization at hydrothermal conditions: An 1000 experimental study. Geochemistry, Geophysics, Geosystems 17, 44-55.

1001 Ferry, J.M., 2000. Patterns of mineral occurrence in metamorphic rocks. American 1002 Mineralogist 85, 1573-1588.

1003 Fu, Q., Foustoukos, D.I., Seyfried, W.E., 2008. Mineral catalyzed organic synthesis in 1004 hydrothermal systems: An experimental study using time-of-flight secondary ion mass 1005 spectrometry. Geophysical research letters 35.

1006 Galvez, M.E., Beyssac, O., Martinez, I., Benzerara, K., Chaduteau, C., Malvoisin, B., 1007 Malavieille, J., 2013. Graphite formation by carbonate reduction during subduction. Nature 1008 Geoscience 6, 473-477.

1009 Gautier, Q., 2012. Cinétiques de précipitation de minéraux carbonatés magnésiens, influence 1010 de ligands organiques et conséquences pour la séquestration minérale du CO2. Université 1011 Paris-Est.

1012 Giammar, D.E., Bruant, J.R.G., Peters, C.A., 2005. Forsterite dissolution and magnesite 1013 precipitation at conditions relevant for deep saline aquifer storage and sequestration of carbon 1014 dioxide. Chemical Geology 217, 257-276.

1015 Gislason, S.R., Wolff-Boenisch, D., Stefansson, A., Oelkers, E., Gunnlaugsson, E.,
1016 Sigurdardottir, H., Sigfusson, B., Broecker, W., Matter, J., Stute, M., Axelsson, G.,
1017 Fridriksson, T., 2010. Mineral sequestration of carbon dioxide in basalt: the CarbFix project.
1018 International Journal of Greenhouse Gas Control 4, 537–545.

1019 Godard, M., Luquot, L., Andreani, M., Gouze, P., 2013. Incipient hydration of mantle
1020 lithosphere at ridges: a reactive-percolation experiment. Earth and Planetary Science Letters
1021 371, 92-102.

1022 Grandstaff, D.E., 1978. Changes in surface area and morphology and the mechanism of a
1023 forsterite dissolution. Geochimica et Cosmochimica Acta 42, 1899-1901.

1024 Hänchen, M., Prigiobbe, V., Baciocchi, R., Mazzotti, M., 2008. Precipitation in the Mg-
1025 carbonate system: effects of temperature and CO_2 pressure. Chemical Engineering Science 63,
1026 1012-1028.

1027 Hänchen, M., Prigiobbe, V., Storti, G., Seward, T.M., Mazzoti, M., 2006. Dissolution kinetics
1028 of fosteritic olivine at 90–150°C including effects of the presence of CO_2. Geochimica et
1029 Cosmochimica Acta 70, 4403-4416.

1030 Hansen, L.D., Dipple, G.M., Gordon, T.M., Kellett, D.A., 2005. Carbonated serpentinite
1031 (listwanite) at Atlin, British Columbia: A geological analogue to carbon dioxide sequestration.
1032 The Canadian Mineralogist 43, 225-239.

1033 Horita, J., Berndt, M.E., 1999. Abiogenic methane formation and isotopic fractionation under
1034 hydrothermal conditions. Science 285, 1055-1057.

1035 Jamtveit, B., Malthe-Sørenssen, A., Kostenko, O., 2008. Reaction enhanced permeability
1036 during retrogressive metamorphism. Earth and Planetary Science Letters 267, 620-627.

1037 Javoy, M., Pineau, F., 1991. The volatiles record of a popping rock from the Mid-Atlantic
1038 ridge at 14°N: chemical and isotopic composition of gas trapped in the vesicles. Earth and
1039 Planetary Science Letters 107, 598-611.

1040 Jun, Y.-S., Giammar, D.E., Werth, C.J., 2013. Impacts of geochemical reactions on geologic
1041 carbon sequestration. Environmental Science & Technology 47, 3-8.

1042 Kelemen, P.B., Hirth, G., 2012. Reaction-driven cracking during retrograde metamorphism:
1043 Olivine hydration and carbonation. Earth and Planetary Science Letters 345, 81-89.

1044 Kelemen, P.B., Manning, C.E., 2015. Reevaluating carbon fluxes in subduction zones, what
1045 goes down, mostly comes up. Proceedings of the National Academy of Sciences 112, E3997-
1046 E4006.

1047 Kelemen, P.B., Matter, J., 2008. In situ carbonation of peridotite for CO_2 storage. Proceedings
1048 of the National Academy of Sciences 105, 17295–17300.

1049   Kelemen, P.B., Matter, J., Streit, E.E., Rudge, J.F., Curry, W.B., Blusztajn, J., 2011. Rates
1050   and mechanisms of mineral carbonation in peridotite: natural processes and recipes for
1051   enhanced, in situ CO_2 capture and storage. Annual Review of Earth and Planetary Sciences
1052   39, 546-576.

1053   King, H.E., Satoh, H., Tsukamoto, K., Putnis, A., 2014. Surface-specific measurements of
1054   olivine dissolution by phase-shift interferometry. American Mineralogist 99, 377-386.

1055   Klein, F., Bach, W., Jöns, N., McCollom, T., Moskowitz, B., Berquó, T., 2009. Iron
1056   partitioning and hydrogen generation during serpentinization of abyssal peridotites from 15°N
1057   on the Mid-Atlantic Ridge. Geochimica et Cosmochimica Acta 73, 6868-6893.

1058   Klein, F., McCollom, T.M., 2013. From serpentinization to carbonation: New insights from a
1059 CO_2 injection experiment. Earth and Planetary Science Letters 379, 137-145.

1060   Kuebler, K., 2009. A comparison of iddingsite alteration in two terrestrial basalts and the
1061   ALHA 77005 martian meteorite using Raman spectroscopy and electron microprobe analyses.

1062   Kuebler, K., 2013. A comparison of the iddingsite alteration products in two terrestrial basalts
1063   and the Allan Hills 77005 martian meteorite using Raman spectroscopy and electron
1064   microprobe analyses. Journal of Geophysical Research: Planets (1991–2012) 118, 803-830.

1065   Kuebler, K., Wang, A., Haskin, L.A., Jolliff, B.L., 2003. A study of olivine alteration to
1066   iddingsite using Raman spectroscopy, Lunar and Planetary Institute Science Conference
1067   Abstracts, p. 1953.

1068   Lazar, C., McCollom, T., Manning, C.E., 2012. Abiogenic methanogenesis during
1069   experimental komatiite serpentinization: implications for the evolution of the early
1070   Precambrian atmosphere. Chemical Geology 326, 102-112.

1071   Lee, M.R., Tomkinson, T., Hallis, L.J., Mark, D.F., 2015. Formation of iddingsite veins in the
1072   martian crust by centripetal replacement of olivine: Evidence from the nakhlite meteorite
1073   Lafayette. Geochimica et Cosmochimica Acta 154, 49-65.

1074   Lorne, B., Perrier, F., Avouac, J.-P., 1999. Streaming potential measurements: 1. Properties of
1075   the electrical double layer from crushed rock samples. Journal of Geophysical Research: Solid
1076   Earth (1978–2012) 104, 17857-17877.

1077   Ludwig, K.A., Kelley, D.S., Butterfield, D.A., Nelson, B.K., Früh-Green, G.L., 2006.
1078   Formation and evolution of carbonate chimneys at the Lost City Hydrothermal Field.
1079   Geochimica et Cosmochimica Acta 70, 3625-3645.

1080   Luhmann, A.J., Tutolo, B.M., Bagley, B.C., Mildner, D.F., Scheuermann, P.P., Feinberg,
1081   J.M., Ignatyev, K., Seyfried Jr, W., 2017a. Chemical and physical changes during seawater

1082 flow through intact dunite cores: An experimental study at 150–200° C. Geochimica et

1083 Cosmochimica Acta 214, 86-114.

1084 Luhmann, A.J., Tutolo, B.M., Tan, C., Moskowitz, B.M., Saar, M.O., Seyfried, W.E., 2017b.

1085 Whole rock basalt alteration from CO_2-rich brine during flow-through experiments at 150 ° C

1086 and 150 bar. Chemical Geology 453, 92-110.

1087 Luquot, L., Andreani, M., Gouze, P., Camps, P., 2012. CO_2 percolation experiment through

1088 chlorite/zeolite-rich sandstone (Pretty-Hill Formation – Otway Basin–Australia). Chemical

1089 Geology 294-29, 75-88.

1090 Malvoisin, B., Brunet, F., 2014. Water diffusion-transport in a synthetic dunite: Consequences

1091 for oceanic peridotite serpentinization. Earth and Planetary Science Letters 403, 263-272.

1092 Malvoisin, B., Brunet, F., Carlut, J., Rouméjon, S., Cannat, M., 2012. Serpentinization of

1093 oceanic peridotites: 2. Kinetics and processes of San Carlos olivine hydrothermal alteration.

1094 Journal of Geophysical Research 117.

1095 Mao, S., Duan, Z., 2009. The viscosity of aqueous alkali-chloride solutions up to 623 K, 1000

1096 bar and high ionic strength. International Journal of Thermophysics 30, 1510-1523.

1097 Martinez, I., Vacquand, C., Kularatne, K., Sissmann, O., Milesi, V., Bernard, S., 2017.

1098 Formation of reduced carbon compounds using natural catalysts in hydrothermal experiments,

1099 Goldschmidt Abstract, 2602.

1100 Matter, J.M., Kelemen, P.B., 2009. Permanent storage of carbon dioxide in geological

1101 reservoirs by mineral carbonation. Nature Geoscience 2, 837-841.

1102 McCollom, T.M., 2016. Abiotic methane formation during experimental serpentinization of

1103 olivine. Proceedings of the National Academy of Sciences 113, 13965-13970.

1104 McGrail, B.P., Spane, F.A., Sullivan, E.C., Bacon, D.H., Hund, G., 2011. The Wallula basalt

1105 sequestration pilot project. Energy Procedia 4, 5653-5660.

1106 Ménez, B., Pasini, V., Brunelli, D., 2012. Life in the hydrated suboceanic mantle. Nature

1107 Geoscience 5, 133-137.

1108 Milesi, V., McCollom, T.M., Guyot, F., 2016. Thermodynamic constraints on the formation

1109 of condensed carbon from serpentinization fluids. Geochimica et Cosmochimica Acta 189,

1110 391-403.

1111 Nakamura, K., Kato, Y., 2004. Carbonatization of oceanic crust by the seafloor hydrothermal

1112 activity and its significance as a CO_2 sink in the early Archean. Geochimica et Cosmochimica

1113 Acta 68, 4595-4618.

Nasir, S., Sayigh, A., Razak, A., Al Harthy, A., Al-Khirbash, S., Al-Jaaidi, O., Musllam, A., Al-Mishwat, A., Al-Bu'saidi, S., 2007. Mineralogical and geochemical characterization of listwaenite from the Semail ophiolite, Oman. Chemie Der Erde-Geochemistry 67, 213-228.

Noël, J., Godard, M., Oliot, E., Martinez, I., Williams, M., Boudier, F., Rodriguez, O., Chaduteau, C., Escario, S., Gouze, P., 2018. Evidence of polygenetic carbon trapping in the Oman Ophiolite: Petro-structural, geochemical, and carbon and oxygen isotope study of the Wadi Dima harzburgite-hosted carbonates (Wadi Tayin massif, Sultanate of Oman). Lithos.

Oelkers, E.H., Gislason, S.R., Matter, J., 2008. Mineral carbonation of CO_2. Elements 4, 333-337.

Parkhurst, D.L., Appelo, C.A.J., 2013. Description of Input and Examples for PHREEQC Version 3--a Computer Program for Speciation, Batch-reaction, One-dimensional Transport, and Inverse Geochemical Calculations: Ch. A43. U.S. Geological Survey Techniques and Methods book 6. USGS.

Paterson, M.S., 1990. Rock deformation experimentation. Geophysical monograph series 56, 187-194.

Peuble, S., Andreani, M., Godard, M., Gouze, P., Barou, F., Van De Moortèle, B., Mainprice, D., Reynard, B., 2015a. Carbonate mineralization in percolated olivine aggregates: Linking effects of crystallographic orientation and fluid flow. American Mineralogist 100, 474-482.

Peuble, S., Andreani, M., Gouze, P., Pollet-Villard, M., Reynard, B., Van de Moortele, B., 2017. Multi-scale characterization of the incipient carbonation of peridotite. Chemical Geology 476, 150-160.

Peuble, S., Godard, M., Luquot, L., Andreani, M., Martinez, I., Gouze, P., 2015b. CO_2 geological storage in olivine rich basaltic aquifers: New Insights from flow-through experiments. Applied Geochemistry 52, 174-190.

Pineau, F., Javoy, M., 1994. Strong degassing at ridge crests: the behaviour of dissolved carbon and water in basalt glasses at 14°N, Mid-Atlantic ridge. Earth and Planetary Science Letters 123, 179-184.

Pokrovsky, O.S., Schott, J., 2000. Kinetics and mechanism of forsterite dissolution at 25°C and pH from 1 to 12. Geochimica et Cosmochimica Acta 64, 3313–3325.

Pokrovsky, O.S., Schott, J., 2002. Surface chemistry and dissolution kinetics of divalent metal carbonates. Environmental Science & Technology 36, 426-432.

Prigiobbe, V., Costa, G., Baciocchi, R., Hänchen, M., Mazzotti, M., 2009. The effect of CO_2 and salinity on olivine dissolution kinetics at 120°C. Chemical Engineering Science 64, 3510-3515.

1148 Rausch, S., Böhm, F., Bach, W., Klügel, A., Eisenhauer, A., 2013. Calcium carbonate veins in

1149 ocean crust record a threefold increase of seawater Mg/Ca in the past 30 million years. Earth

1150 and Planetary Science Letters 362, 215-224.

1151 Rividi, N., Van Zuilen, M., Philippot, P., Menez, B., Godard, G., Poidatz, E., 2010.

1152 Calibration of carbonate composition using micro-Raman analysis: application to planetary

1153 surface exploration. Astrobiology 10, 293-309.

1154 Rosso, J.J., Rimstidt, J.D., 2000. A high resolution study of forsterite dissolution rates.

1155 Geochimica et Cosmochimica Acta 64, 797-811.

1156 Rudge, J.F., Kelemen, P.B., Spiegelman, M., 2010. A simple model of reaction-induced

1157 cracking applied to serpentinization and carbonation of peridotite. Earth and Planetary

1158 Science Letters 291, 215-227.

1159 Saldi, G., Schott, J., Pokrobsky, O., Gautier, Q., Oelkers, E., 2012. An experimental study of

1160 magnesite precipitation rates at neutral to alkaline conditions and 100-200°C as a function of

1161 pH, aqueous solution composition and chemical affinity. Geochimica et Cosmochimica Acta

1162 83, 93-109.

1163 Saldi, G.D., Jordan, G., Schott, J., Oelkers, E.H., 2009. Magnesite growth rates as a function

1164 of temperature and saturation state. Geochimica et Cosmochimica Acta 73, 5646-5657.

1165 Schott, J., Pokrovsky, O.S., Oelkers, E.H., 2009. The link between mineral

1166 dissolution/precipitation kinetics and solution chemistry. Reviews in Mineralogy &

1167 Geochemistry 70, 207-258.

1168 Schwarzenbach, E.M., Früh-Green, G.L., Bernasconi, S.M., Alt, J.C., Plas, A., 2013.

1169 Serpentinization and carbon sequestration: A study of two ancient peridotite-hosted

1170 hydrothermal systems. Chemical Geology 351, 115-133.

1171 Schwarzenbach, E.M., Gill, B.C., Gazel, E., Madrigal, P., 2016. Sulfur and carbon

1172 geochemistry of the Santa Elena peridotites: Comparing oceanic and continental processes

1173 during peridotite alteration. Lithos 252, 92-108.

1174 Seifritz, W., 1990. CO_2 disposal by means of silicates. Nature 345, 486.

1175 Sforna, M.C., Brunelli, D., Pisapia, C., Pasini, V., Malferrari, D., Ménez, B., 2018. Abiotic

1176 formation of condensed carbonaceous matter in the hydrating oceanic crust. Nature

1177 Communications 9, 5049.

1178 Sissmann, O., Brunet, F., Martinez, I., Guyot, F., Verlaguet, A., Pinquier, Y., Daval, D., 2014.

1179 Enhanced olivine carbonation within a basalt as compared to single-phase experiments:

1180 reevaluating the potential of CO_2 mineral sequestration. Environmental Science &

1181 Technology.

1182 Steefel, C.I., DePaolo, D.J., Lichtner, P.C., 2005. Reactive transport modeling: an essential
1183 tool and a new research approach for the Earth sciences. Earth and Planetary Science Letters
1184 240, 539-558.

1185 Tutolo, B.M., Luhmann, A.J., Tosca, N.J., Seyfried, W.E., 2018. Serpentinization as a
1186 reactive transport process: The brucite silicification reaction. Earth and Planetary Science
1187 Letters 484, 385-395.

1188 Van Der Lee, J., De Windt, L., 2001. Present state and future directions of modeling of
1189 geochemistry in hydrogeological systems. Journal of Contaminant Hydrology 47, 265-282.

1190 Van der Lee, J., De Windt, L., Lagneau, V., Goblet, P., 2003. Module-oriented modeling of
1191 reactive transport with HYTEC. Computers and Geosciences 29, 265–275.

1192 Velbel, M.A., 2009. Dissolution of olivine during natural weathering. Geochimica et
1193 Cosmochimica Acta 73, 6098-6113.

1194 Velbel, M.A., Ranck, J.M., 2008. Etch pits on naturally altered olivine from dunites of the
1195 Appalachian Blue Ridge Mountains, North Carolina, USA. Mineralogical Magazine 72, 145-
1196 148.

1197 Wogelius, R.A., Walther, J.V., 1990. Olivine dissolution at 25°C: effects of pH, CO_2, and
1198 organic acids. Geochimica et Cosmochimica Acta 55, 943-954.

1199 Yeghicheyan, D., Bossy, C., Coz, M.B., Douchet, C., Granier, G., Heimburger, A., Lacan, F.,
1200 Lanzanova, A., Rousseau, T., Seidel, J.-L., 2013. A compilation of Silicon, Rare Earth
1201 Element and twenty-one other Trace Element concentrations in the Natural River Water
1202 Reference Material SLRS-5 (NRC-CNRC). Geostandards and Geoanalytical Research.

1203 Zeebe, R.E., Caldeira, K., 2008. Close mass balance of long-term carbon fluxes from ice-core
1204 CO_2 and ocean chemistry records. Nature Geoscience 1, 312-315.

Table

Experimental conditions (T = 185°C)			
Experiments	SC1-L	SC2-M	SC3-H
Duration of experiments (hours)	92.88	156.36	333.34
Total pressure (MPa)	25.0	25.0	20.0
CO_2 partial pressure (MPa)	0.1	1.0	10.0
CO_2 (mmol.L^{-1})	6.26	62.6	659.7
Initial magnetic susceptibility (10^{-8} m^3.Kg^{-1})	16.9	17.6	19.2
Final magnetic susceptibility (10^{-8} m^3.Kg^{-1})	16.9	17.4	21.8
Initial porosity (%)	10.96	11.30	10.57
Initial permeability (10^{-15} m²)	1.876	1.561	4.589
Final permeability (10^{-15} m²)	0.075	0.019	0.005

	SC1-L	SC2-M	SC3-H
Duration of experiments (hours)			
Total pressure (MPa)			
CO_2 partial pressure (MPa)			

Table 1

Peuble et al., 2018

ICP-MS data	Det. Limit	Injected fluid
Si (ppm)	0.815	14.95
Mg	0.001	8.73
Fe	0.005	0.01
Ca	0.012	12.1

ICP-MS data	Det. Limit	Injected fluid
Si (ppm)	0.815	14.95
Mg	0.001	8.73
Fe	0.005	0.01
Ca	0.012	12.1

Table 2
Peuble et al., 2018

Bulk rock analyses (wt.%)	Initial olivine powder	SC2-M	SC3-H
H_2O	0.04	0.08	n.a.
CO_2 inorganic	< 0.05	0.10	1.31
CO_2 organic*	< 0.05	0.17	0.04
CO_2 total	< 0.05	0.27	1.35

*Note. n.a.: not analyzed ; *organic carbon recalculated as CO_2*

Table 3
Peuble et al., 2018

Mass balance calculations		SC1-L	SC2-M	SC3-H
Mass Variation. $\Delta m/m_0$ in %	Dissolved olivine	-0.48	-3.69	-4.31
	Hydrous phases	0.40	3.15	0.50
	Carbonates	0.08	0.58	3.12
	Carbon	0.01	0.10	0.01
	Total	0.01	0.14	-0.68
	H_2O	0.18	1.44	0.10
	CO_2 inorganic	0.03	0.22	1.61
	CO_2 organic*	0.04	0.38	0.05
	CO_2 total	0.07	0.60	1.66
Porosity changes. ϕ/ϕ_0	Calcite & Brucite	0.99	0.88	-
	Calcite & Serpentine	0.99	0.91	-
	Siderite & Brucite	0.99	0.89	-
	Siderite & Serpentine	0.99	0.93	-
	Magnesite & Goethite	-	-	1.05
	Magnesite & Serpentine	-	-	1.03

*Note: (-) loss & (+) gain ; *organic carbon recalculated as CO_2*

Table 4
Peuble et al., 2018
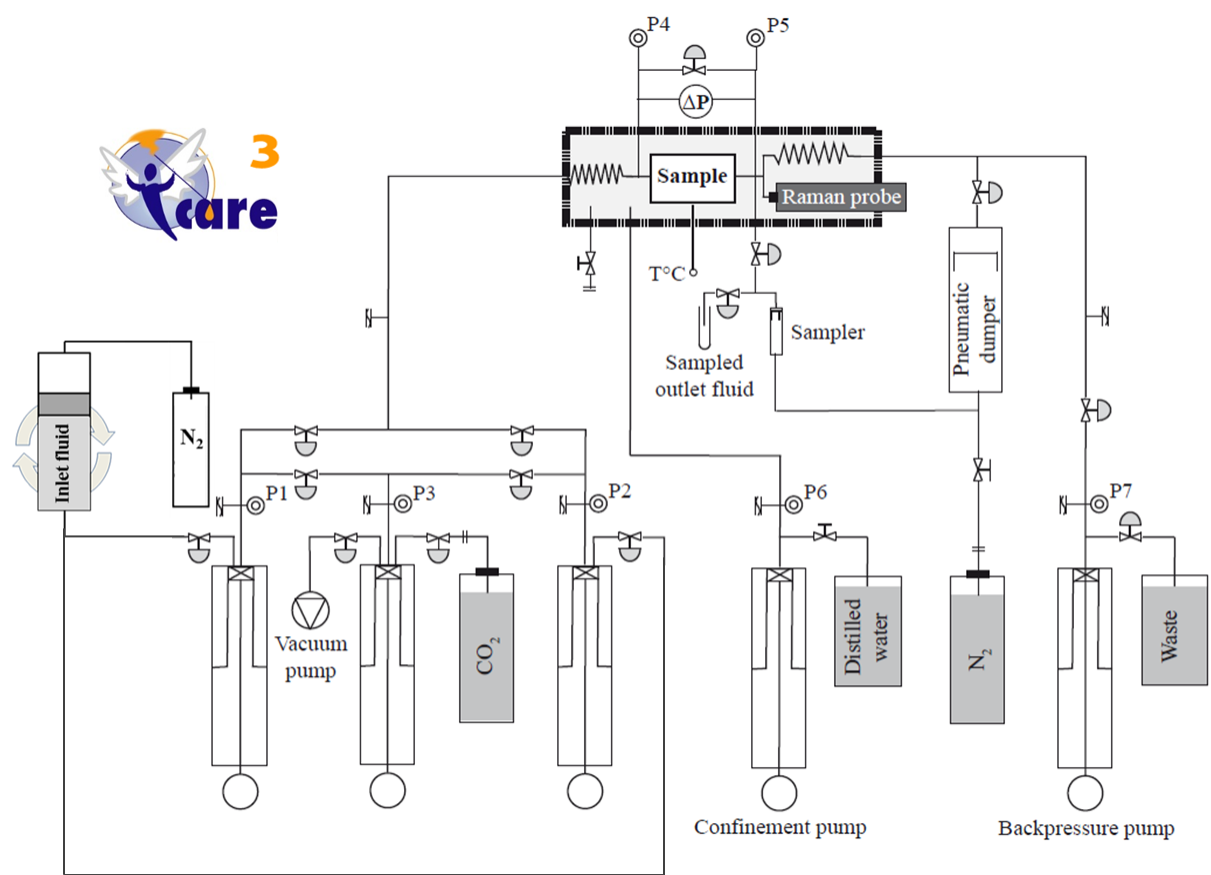
Figure

Figure 1. Peuble et al. 2018
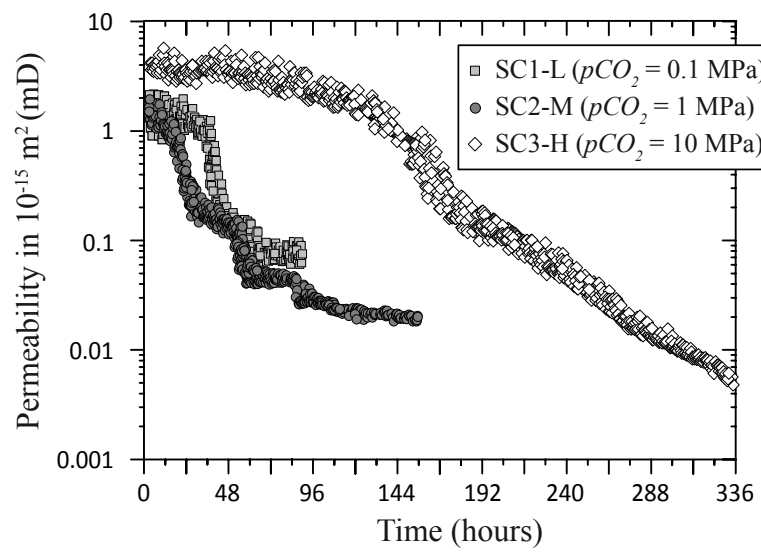
Figure 2. Peuble et al. 2018

Figure 3. Peuble et al. 2018

a

1 mm

b

Fluid flow

1 mm

c

Fig.8

Fluid flow

1 mm

d

Fluid flow

1 mm
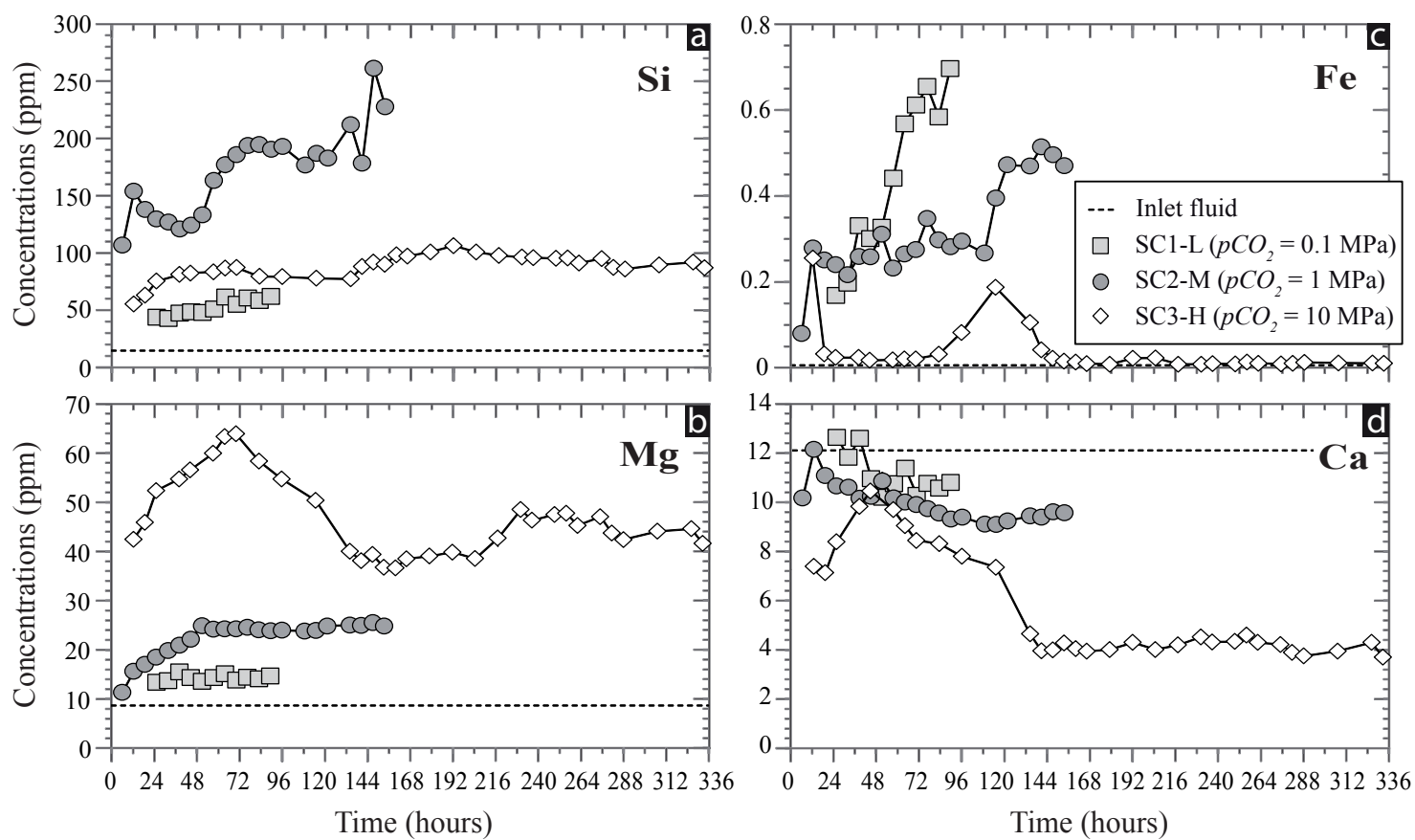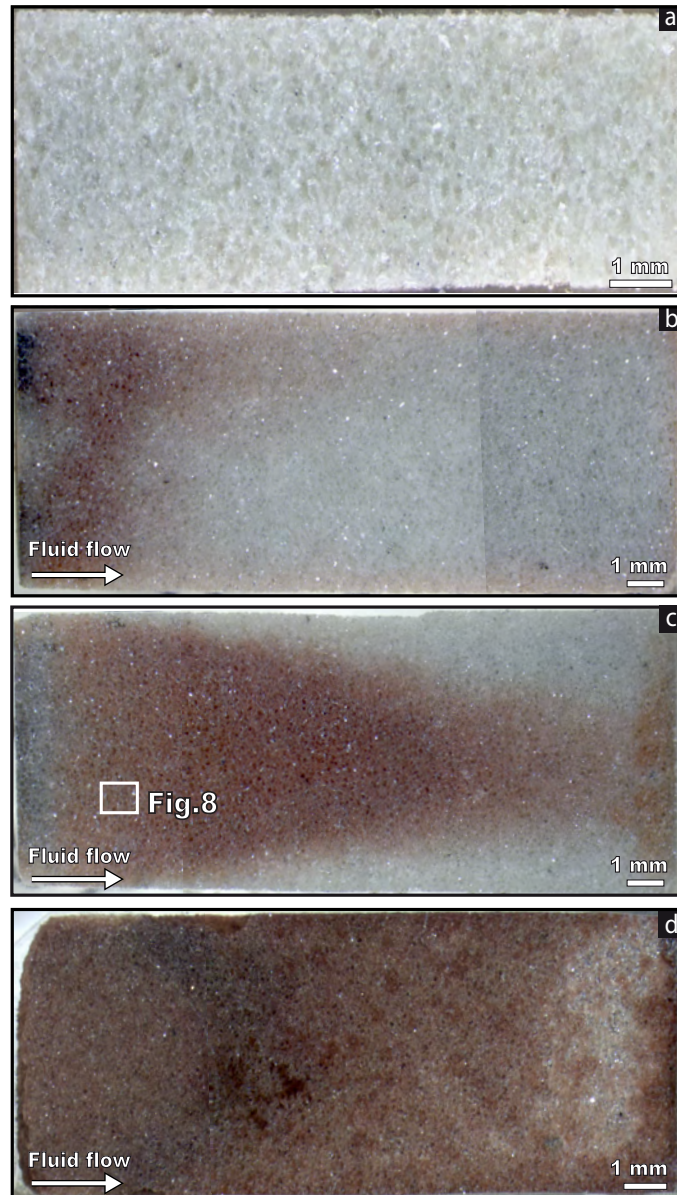
Figure 4. Peuble et al. 2018
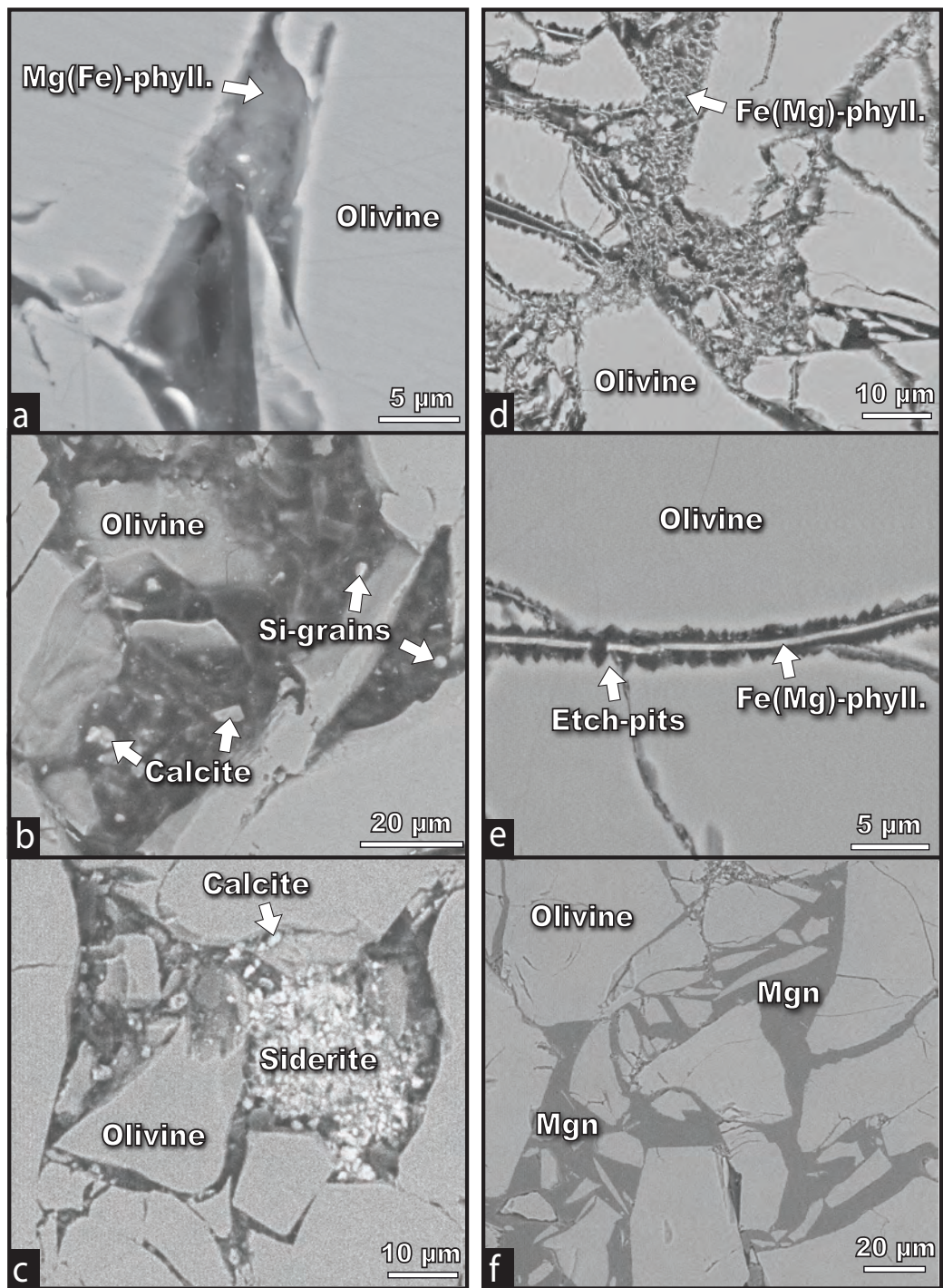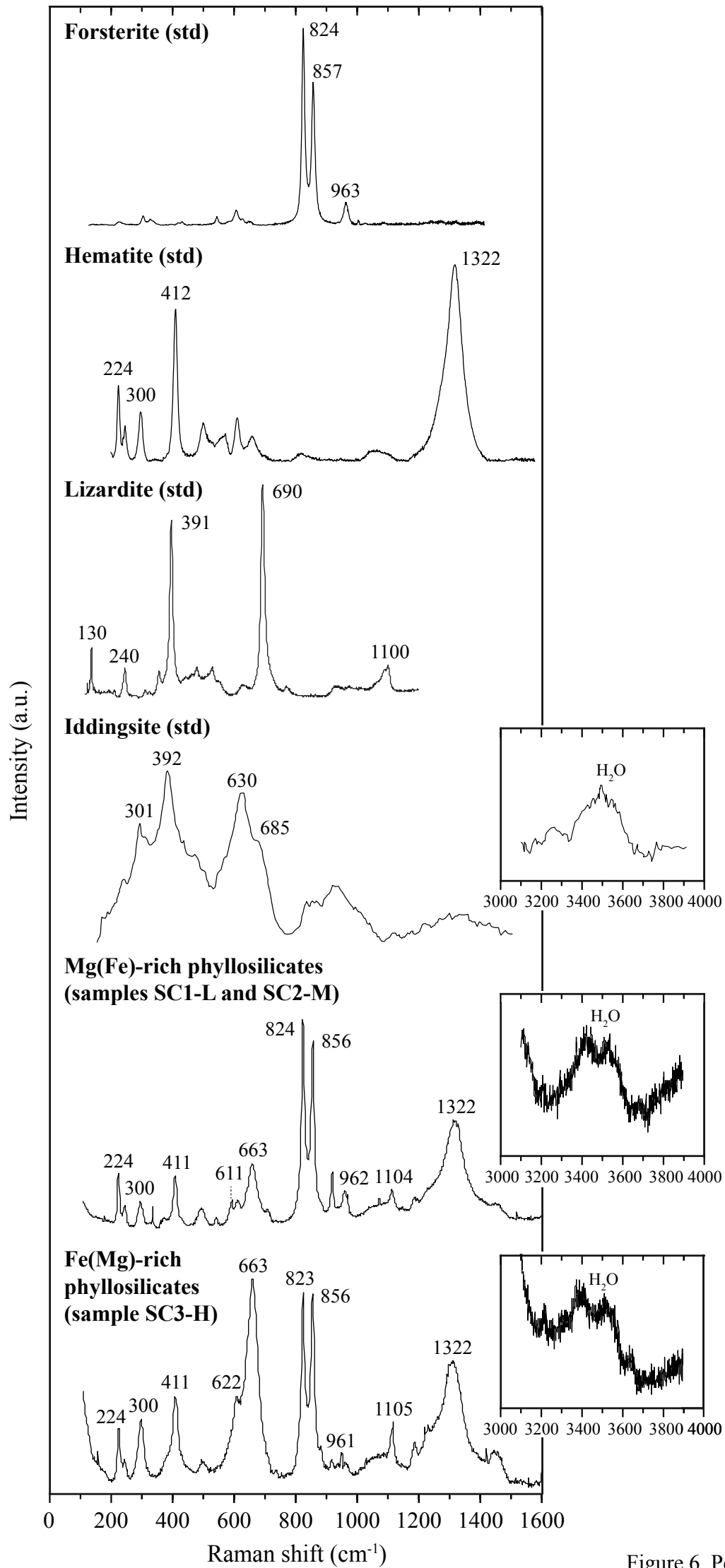
Figure 5. Peuble et al. 2018
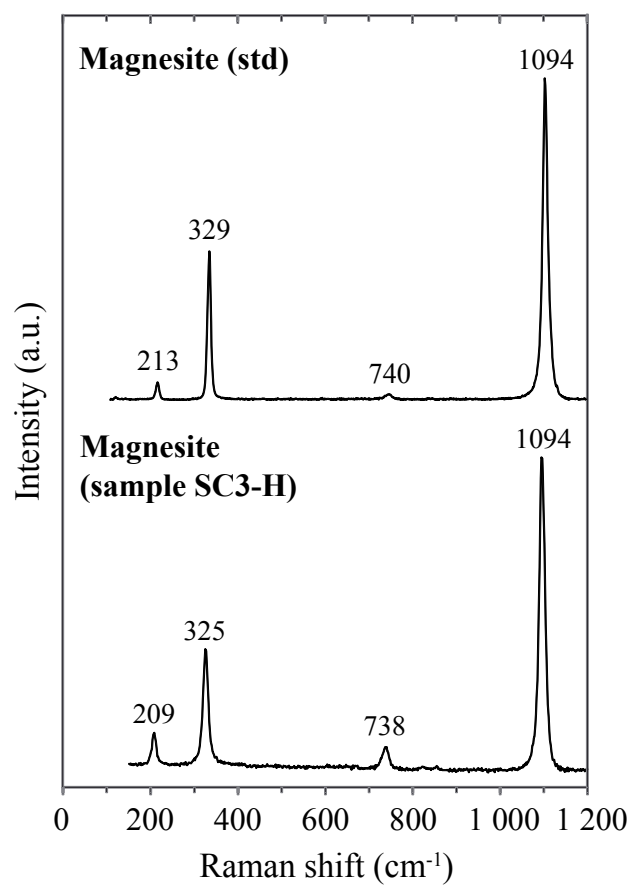
Figure 6. Peuble et al. 2018
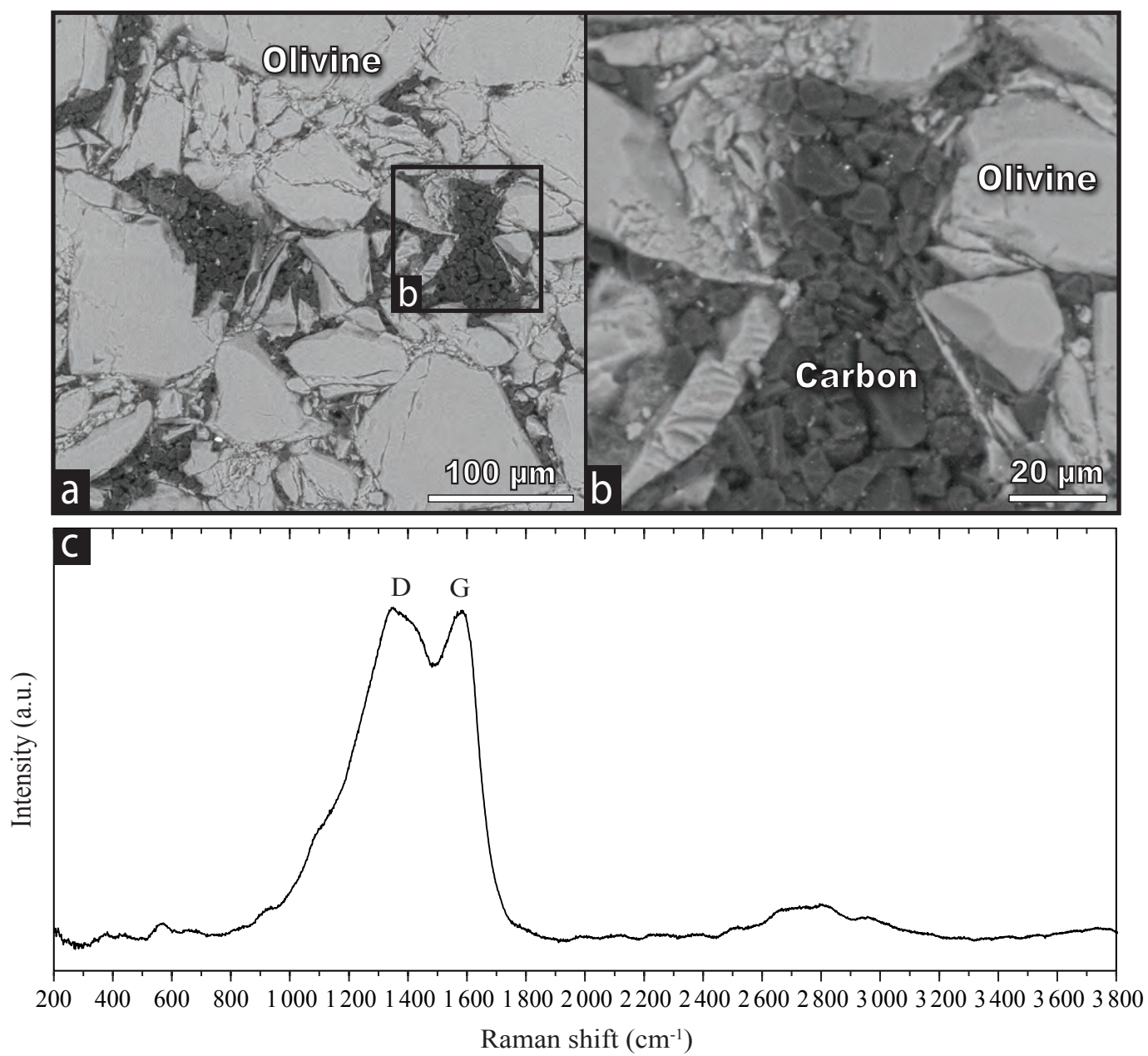
Figure 7. Peuble et al. 2018
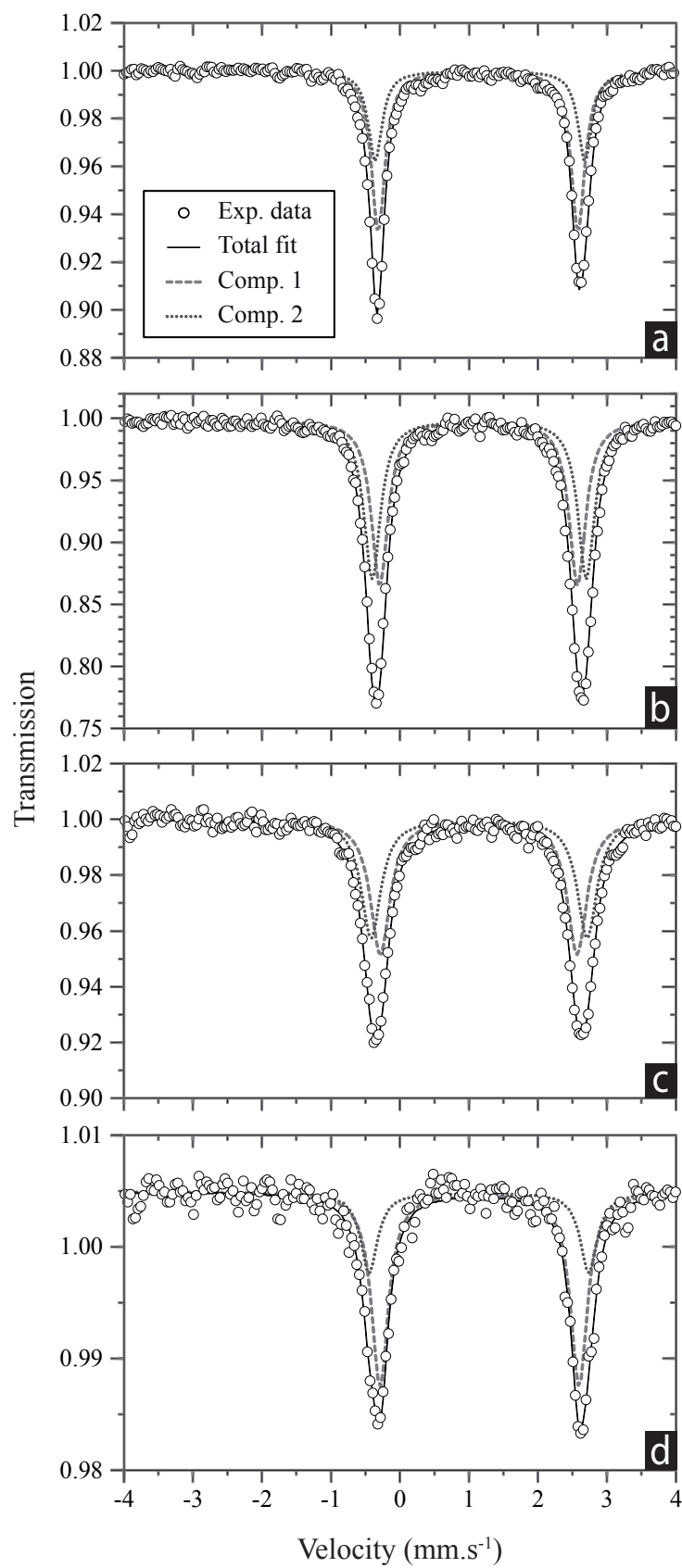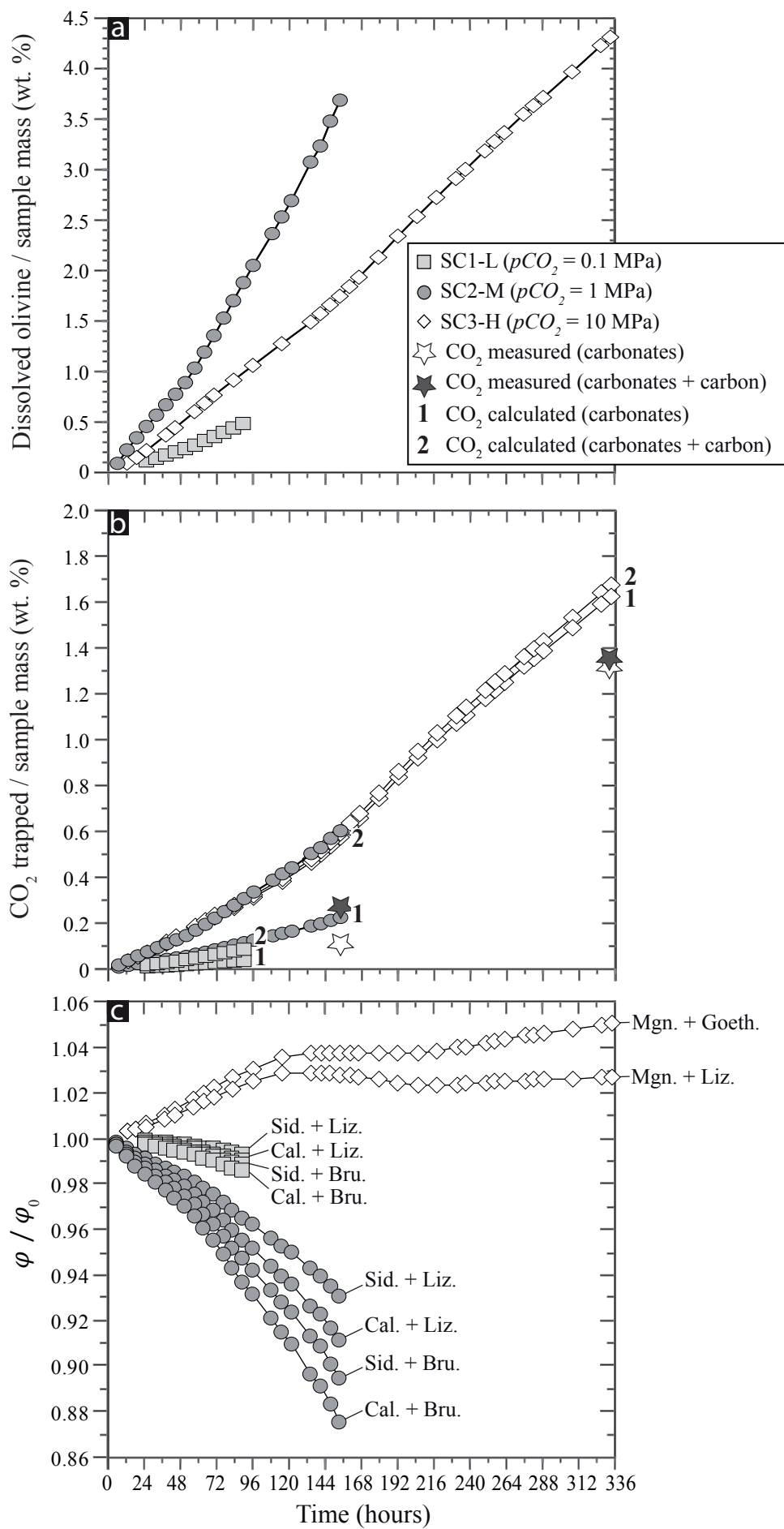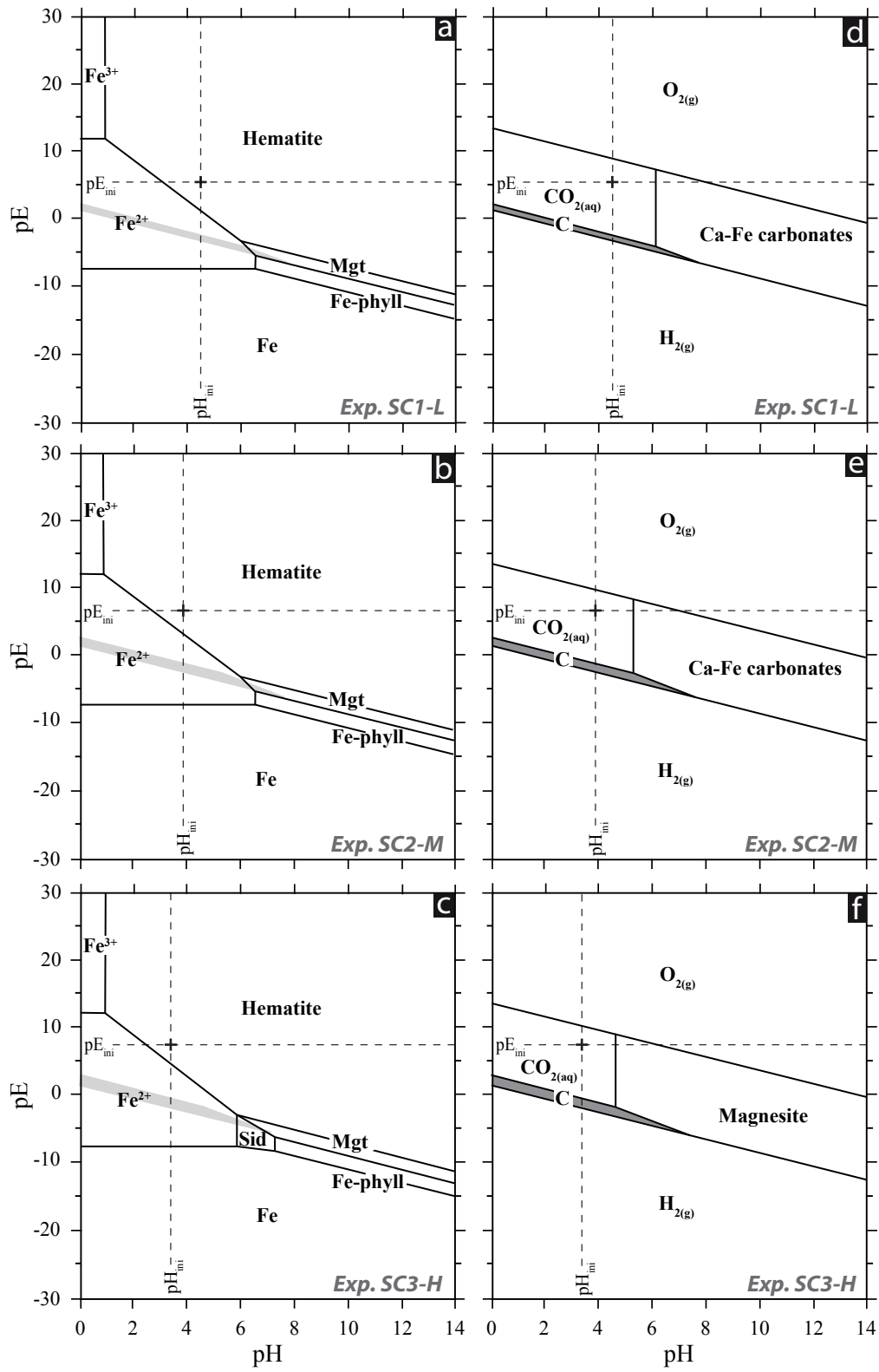
Figure 8. Peuble et al. 2018

Figure 9. Peuble et al. 2018

Figure 10. Peuble et al. 2018

Figure 11. Peuble et al. 2018